ELSEVIER

Journal of Volcanology and Geothermal Research 101 (2000) 27–65

Journal of volcanology and geothermal research

www.elsevier.nl/locate/jvolgeores

Analysis of seismic and acoustic observations at Arenal Volcano, Costa Rica, 1995–1997

M.T. Hagerty[a,b,*], S.Y. Schwartz[a], M.A. Garcés[c], M. Protti[d]

[a]*Institute of Tectonics, University of California, Santa Cruz, CA, USA*
[b]*Now at Lamont-Doherty Earth Observatory, Columbia University, Palisades, NY, USA*
[c]*Aso Volcanological Laboratory, Kyoto University, Japan*
[d]*Observatorio Vulcanológico y Sismológico, Universidad Nacional, Costa Rica*

Received 30 November 1999

Abstract

In November 1995, we installed five, three-component broadband seismometers and electronic tiltmeters around the circumference of Arenal Volcano, a young stratovolcano in Costa Rica that exhibits strombolian activity. With the addition of two continuous-recording GPS receivers deployed in May 1995, these instruments provide continuous monitoring of seismicity and ground deformation at an active volcano over a very wide bandwidth. In addition, during April–May 1997, we deployed a small, linear array of co-located three-component seismometers and broadband microphones. This paper presents a comprehensive analysis of all the seismic and acoustic data collected thus far. Seismic signals are primarily of two types: (1) long-period (1–3 Hz) transients associated with summit explosions; and (2) harmonic tremor that contains regularly spaced spectral peaks (0.9, 1.8, 2.7, 3.6, 4.5, 5.4, 6.3, and 7.1 Hz) and lasts up to several hours. The explosion signals appear to originate in a small volume that is located at shallow depth beneath the vent and does not migrate with time. No unambiguous long-period seismic signals ($T > 5$ *s*)associated with volcanic processes at Arenal have been observed during the three-year deployment period. The spectra of summit explosions show distinct signatures at each site, suggesting significant path and/or site modification of the waveforms. In contrast, the harmonic tremor signals show no variation in the frequency content at the five sites, nor on the three seismic components at each site (Hagerty et al., 1997). This, and the fact that harmonic tremor is recorded in the acoustic channels as well, demonstrates that harmonic tremor is not a seismic propagation effect and that pressure disturbances propagate within the magma–gas mixture inside of volcanic conduits. These pressure waves are sensitive to the flow velocity and to small changes in the gas content of the magma–gas mixture. Observations and synthetic tests are presented that challenge the notion that harmonic tremor is a superposition of repeated gas explosions at shallow depth. We propose that equilibrium degassing of the melt creates a stable, stratified magma column where the void fraction increases with decreasing depth and that disruption of this equilibrium stratification is responsible for observed variations in the seismic efficiency of explosions.

Keywords: volcano seismology; volcano acoustics; Arenal Volcano; Costa Rica

1. Introduction

Arenal is a small stratovolcano located in north-central Costa Rica. It is the youngest (3000 years old, Borgia et al., 1988) cone of the Arenal–Chato

* Corresponding author. Fax: + 1-914-365-8150.
E-mail address: mth@ldeo.columbia.edu (M.T. Hagerty).

0377-0273/00/$ - see front matter
PII: S0377-0273(00)00162-1

system, a 12-km-long SE–NW-trending volcanic alignment located at the offset between two linear trends of active volcanoes, the Cordillera de Guanacaste to the northwest and the Cordillera Central to the southeast. Within the Arenal–Chato system, volcanic activity has migrated from Cerro Los Perdidos, an eroded volcanic complex, to Cerro Chato, a truncated cone, to Arenal, the present site of activity. Arenal was considered extinct prior to its violent Plinian eruption in July of 1968, which killed 78 people and opened three craters on its western flank along a WSW lineament. This three-day explosive eruption graded into an effusive phase during which some 6×10^6 m^3 of andesitic–basaltic lava flowed, primarily from the lowest crater (Borgia et al., 1988). In 1984 volcanic activity migrated to the summit crater as Arenal entered a new strombolian phase characterized by frequent summit explosions with continued but diminished block lava flows. Shortly after the catastrophic 1968 eruption, Minakami et al. deployed three short-period seismometers for one month at Arenal and recorded volcano-tectonic and volcano earthquakes which they located beneath Cerro Chato and Arenal, respectively (Minakami et al., 1969). However, the exact locations of these events were not published and, due to the poor geographical distribution of the stations (all were east of the volcano), are probably not well determined. A later field experiment found that the number of earthquakes recorded gradually increased prior to a large eruption on 17 June 1975 (Matumoto and Umana, 1976). More recent field experiments at Arenal have consisted of short-term deployments of a single seismometer (e.g. Melson, 1989; Benoit and McNutt, 1997). A database of accurately located events is essential to examine possible links between seismicity and eruptivity at Arenal and to assess the use of seismicity as an eruption forecaster. Since 1995 we have engaged in a long-term effort of continuous seismic and geodetic monitoring at Arenal in order to characterize the locations and geometries of seismic and geodetic sources and to assess possible links between changes in these and Arenal's eruptive behavior. In addition, during April–May 1997, we deployed a temporary linear array of seismometers and acoustic microphones in order to constrain better the seismic and acoustic wavefields. This paper describes our instrument deployments at Arenal and presents a summary analysis of the seismic and acoustic data collected thus far. Analysis of potential long-term periodicities contained in the seismic signal is currently underway and will be the subject of another paper.

2. Description of deployments

2.1. Broadband network

In May, 1995, we installed two GPS receivers, continuously sampling every 30 s, on the north and south flanks of the volcano. In November, 1995, we established five observation sites around the circumference of the volcano, two of which were chosen to coincide with the continuous GPS sites, and a third, to coincide with the location of a permanent short-period seismometer used to monitor seismicity in the Arenal region by the Costa Rica Volcanological and Seismological Observatory (OVSICORI). Each site is equipped with an STS-2 broadband, three-component (vertical, north, east) seismometer mounted on a concrete pier buried 1–2 m beneath the surface. The seismic data are sampled continuously at a frequency of 20 Hz and written to a local disk. In addition, each site is equipped with an electronic bubble-type tiltmeter, with tilt axis oriented radially with respect to the summit. GPS clocks provide local time corrections. The observation stations (Fig. 1) were sited as close as possible to the summit in light of Arenal's extreme topography and frequent eruptions. The broadband data has been recorded continuously for the last three years.

2.2. Temporary seismic-acoustic array

In addition to the broadband network described above, during April–May 1997, we deployed a temporary array of three-component short-period seismometers co-located with broadband acoustic microphones (Fig. 1). The acoustic sensors consisted of two Brüel and Kjær low-frequency condenser microphones (B&K type 4193) and a Setra microbarometer (model 270). The frequency range of the condenser microphones is between 0.13 Hz and 20 kHz. Their sensitivity is 2.3 mV/Pa with a low-frequency adaptor in place, which extends the frequency response down to 0.07 Hz, and 14.14 mV/Pa without the adaptor. The microbarometer is an

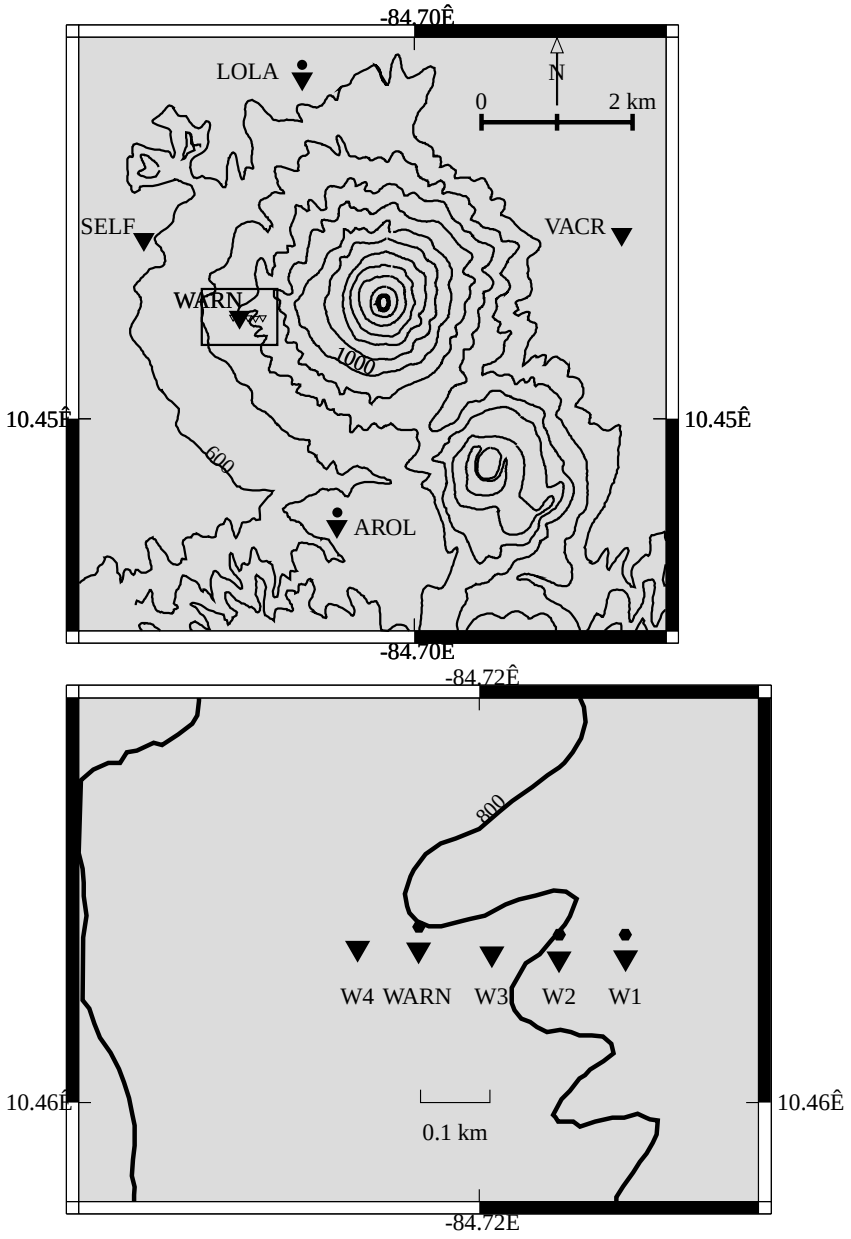

Fig. 1. Top: map of Arenal Volcano showing topographic contours (100 m interval), broadband observation sites (inverted triangles), and continuous GPS receivers (circles). Bottom: inset map showing temporary radial array of seismometers (inverted triangles) and microphones (hexagons).

absolute pressure sensor with response down to DC and a sensitivity of 0.2 mV/Pa. The seismic array consisted of four Mark Products L-22D, three-component seismometers and the broadband seismometer at WARN (Fig. 1). These instruments have a standard frequency of 2.0 Hz and a nominal sensitivity of approximately 100 V/cm/s. Above about 4 Hz their velocity response is essentially flat. While the L22s

do not have the sensitivity nor the recording fidelity of broadband seismometers, they proved quite adequate to record the predominantly 1–4 Hz signals at Arenal. Inclusion of the broadband seismometer at WARN during the array experiment ensures detection of any low-frequency seismic signals and provides a link between the experiment and the 1995–1998 long-term broadband monitoring.

The L22s and the acoustic sensors were deployed in a radial profile with respect to the summit, with 100 m spacing (Fig. 1), chosen as an optimal compromise between array density and array aperture. The array consisted of three L22s (sites W1–W3, Fig. 1) deployed upslope, between site WARN and the summit, and a fourth (W4) deployed downslope from WARN, for a total array length of 400 m. The condenser microphones were deployed at sites W1 and WARN, while the microbarometer was deployed at site W2, forming a 300-m, unevenly spaced acoustic array (Fig. 1). The acoustic and seismic sensors were recorded continuously at 40 Hz.

3. Overview of seismic signals

Fig. 2 is a plot of four consecutive hours of the vertical component of ground velocity recorded at station WARN, approximately 2 km from the summit. Beneath each hour-long seismic trace is a corresponding spectrogram showing the power spectral density as a function of time. The spectrograms are generated by Fourier transforming 10 s triangular windows of data, shifted in 5 s steps. The spectrograms for each hour are independently log-normalized to a maximum amplitude of 0 dB and plotted with a grey scale. The most striking feature of Fig. 2 is the pronounced harmonic tremor with a fundamental frequency (first harmonic) near 0.9 Hz and up to ten harmonics within the 10 Hz Nyquist frequency. During this period the second harmonic peak near 1.8 Hz is the largest. The harmonic spectral content and the phenomena of "gliding'' seen in Fig. 2, whereby the ensemble of spectral peaks shift frequencies as a function of time while maintaining their regular spacing, are very similar to reported tremor features at Langila Volcano, Papua New Guinea (Mori et al., 1989) and Mt. Semeru, Indonesia (Schlindwein et al., 1995). Superimposed on this background tremor are transient events produced by summit explosions that occur roughly every half-hour. The explosion waveforms display the spindle-shaped envelopes and narrowband (1–3 Hz) frequencies characteristic of long-period (LP) events reported for many volcanoes throughout the world (Chouet, 1996). The four hours of data shown in Fig. 2 are by no means anomalous; Arenal generates nearly continual volcanic tremor which is principally harmonic, and much of the data we have recorded over the past three years appears qualitatively similar to Fig. 2. Although recent deployments of broadband seismometers at active volcanoes elsewhere have reported ultra or very LP signals (period >5 s) [e.g. Aso Volcano (Kawakatsu et al., 1994); Stromboli (Neuberg et al., 1994); Erebus (Rowe et al., 1998)], we have recorded no unambiguous LP energy associated with volcanic processes at Arenal during the entire deployment period. Small-amplitude LP pulses have been observed at Arenal ($T \sim 120$ s) and are believed to be either short duration tilts of the volcano or more likely, a non-linear response of the seismometer to the high-frequency energy in the ground-coupled air waves which causes the seismometer electronic feedback system to reset. In the following sections we examine the seismic and acoustic waveforms in detail, first for several summit explosions, and later, for several episodes of tremor.

4. Summit explosions

4.1. Explosion seismic waveforms

The strombolian activity at Arenal is remarkably regular and consists of summit explosions that eject incandescent fragments and propel ash-laden columns to heights of 0.5–2 km approximately every half-hour. Often a large audible boom is heard at the beginning of an eruption, which sometimes grades into a series of regular puffing sounds toward the end of the eruption. An example of three-component seismograms produced by a summit explosion is shown for two stations in Fig. 3. The explosion seismograms generally contain an emergent P wave onset, however this particular explosion (GMT 95:349:14:59) produced relatively clear P onsets which have been used to improve onset picks for all other explosions

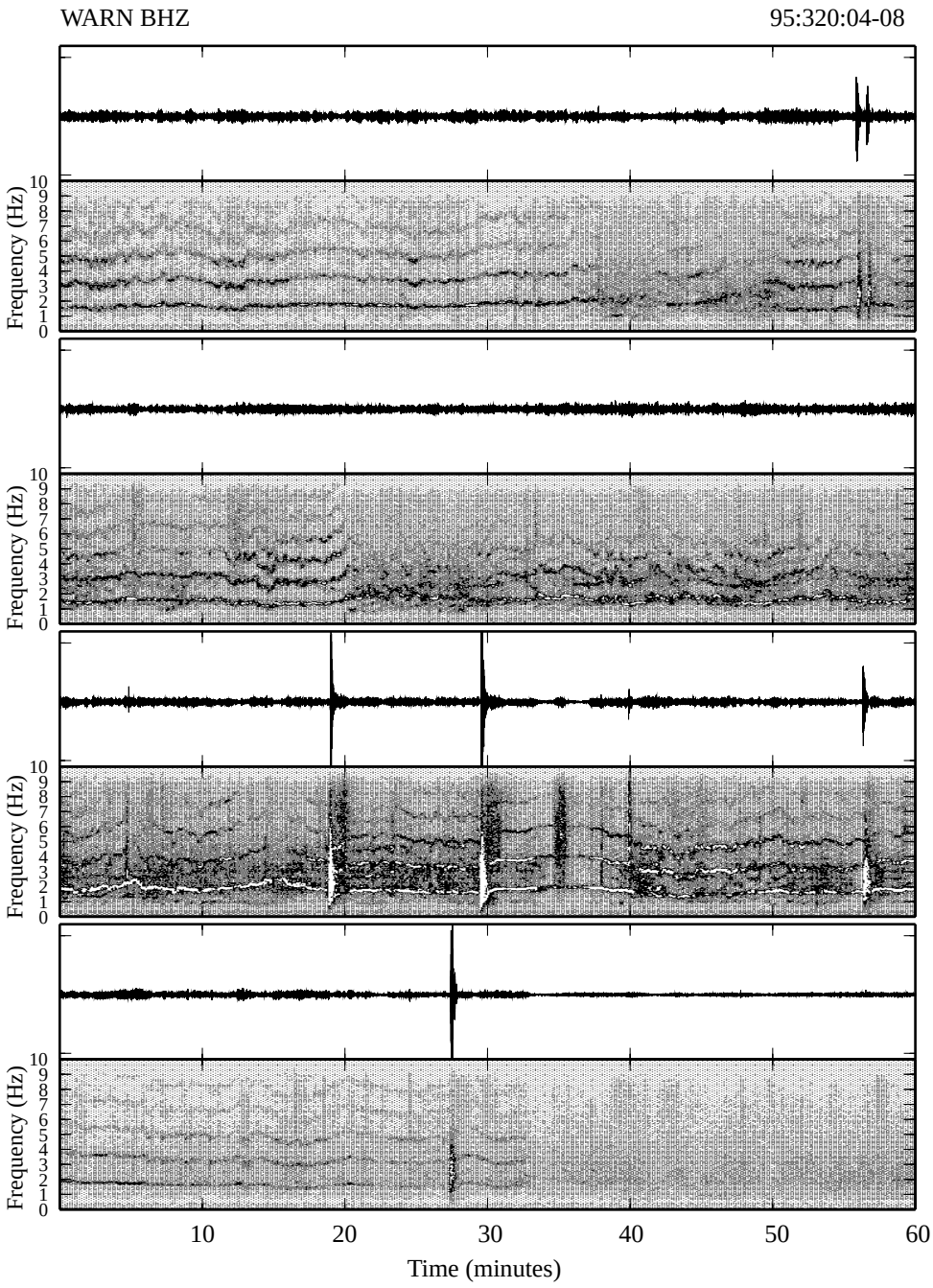

Fig. 2. Four consecutive hours (from top left to bottom right) or normalized vertical component velocity recorded at WARN (95:320:04–95:320:08 GMT). Beneath each hour is a corresponding spectrogram, which is a contour plot of the log of the power spectral density as a function of time. Vertical tic marks denote frequency (0–10 Hz), horizontal tic marks denote time (10 min).

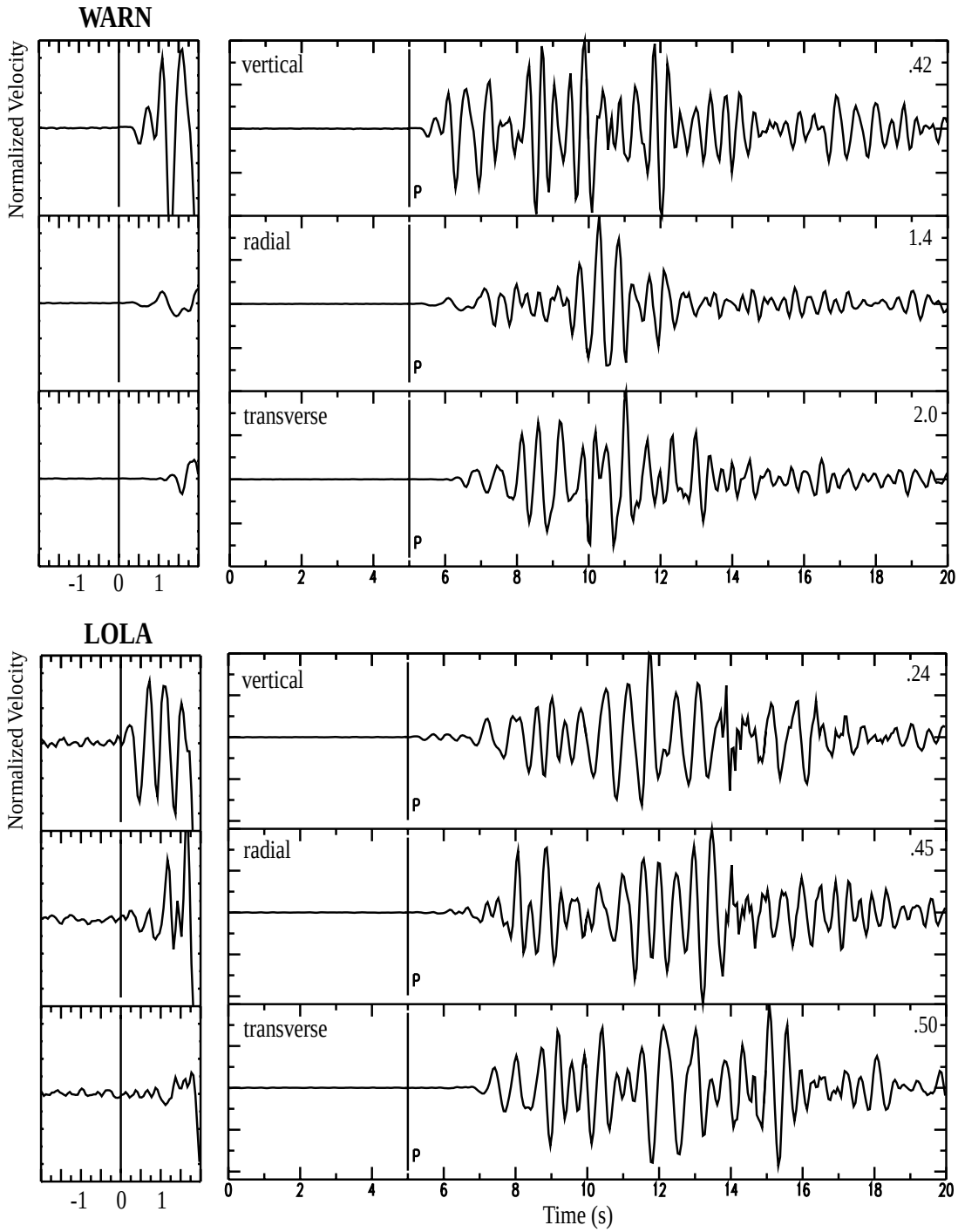

Fig. 3. Three-component velocity seismograms of the “master event” (1995:349:14:59 GMT) recorded at WARN (top and LOLA (bottom). Peak velocities (mm/s) are indicated in the upper right-hand corners. Inset shows close-up of P onset at magnified vertical scale.

through cross-correlation. Explosion first motions are small and upward on both vertical and radial components (see Fig. 3 inset). While the initial vertical and radial energy is in phase, it quickly becomes out of phase and probably represents a complex mix of P-SV waves distorted by propagation through the heterogeneous, and possibly anisotropic, volcanic edifice. Particle motions of explosion seismograms are generally complex and appear to indicate a mix of overlapping body and surface waves. Investigation of seismic profiles have not revealed move-out of any clearly identifiable secondary phases over the distances separating the broadband stations; however, several coherent phases are evident in the more closely spaced linear array profiles and are discussed below.

Fig. 4 shows normalized vertical component velocity seismograms and corresponding Fourier spectral amplitudes recorded at each station. For each station except VACR, 20 explosion waveforms from Julian day 349 (1995) are overlaid. The waveforms for the explosions recorded at each station were cross-correlated with the impulsive explosion waveform for that station (our master event) to improve the picking of emergent P wave onsets. The resulting waveforms, aligned on the adjusted P pick times, overlay nicely; the high degree of waveform correlation suggests that the explosion seismic waves originate in a small source volume. Also, the adjusted P pick times, listed in Table 1 with respect to the adjusted pick time at WARN for each of the events, show little scatter at each station, indicating that the source location is not changing appreciably over time. Station VACR was not operating on Julian day 349, however an impulsive explosion which occurred on Julian day 320 was recorded by VACR and is shown in Fig. 4. The waveform recorded at WARN for the explosion on Julian day 320 is essentially identical to the WARN waveforms for Julian day 349 and has been used to align the VACR waveform with respect to the other stations for Julian day 349. Also shown in Fig. 4 are stacks of the normalized Fourier spectral amplitudes of the waveforms at each station. Most of the explosion seismic energy is concentrated between 1 and 3 Hz. While the waveforms and spectra of the different explosion events are nearly identical at a particular station, they vary greatly from station to station indicating significant path and/or site modification.

4.2. Explosion event location

The average first arrival times for summit explosions on Julian day 349 (Table 1) have been used to locate the explosion source using the hypocentral determination program Hypoellipse (Lahr, 1989). Hypoellipse is able to locate seismic hypocenters in areas of extreme topography, which are typically found in volcanic regions. The top of the velocity model is chosen to coincide with the volcano summit and the stations are embedded in the model at lower elevations. In this way, first arrival times and take-off angles are computed correctly. The apparent velocity estimated using the arrival times in Table 1 is about 3–4 km/s; we selected an optimum half-space P wave velocity of 2.5 km/s to use in the hypocentral determination after performing several preliminary tests with both larger and smaller velocities. Murase and McBirney (1973) measured the compressional velocities as a function of temperature for several igneous samples and found that above about 1000°C, the velocity of all samples converge to 2–3 km/s. Thus, 2.5 km/s is considered a maximum compressional velocity for molten volcanic rocks. Other velocity models, for instance, a 100-m-thick low-velocity layer over a half-space, were found to produce suitably small residual errors; however, the half-space model fits the observations well within the estimated picking errors, hence, there is no need to invoke more complicated velocity structures. The resulting location, shown in Fig. 5, is slightly SE of the summit, at a depth of 0.5 km below sea-level. The offset between the epicenter and the summit is probably not real as topographic contours on Costa Rica maps are known to be offset some 200 m north (M. Protti, personal communication) and the topography of the volcano has changed dramatically since the construction of the contour map. The location root-mean-squares residual time (rms) is 0.02 s, much less than the $\sim$0.06 s precision of the arrival time picks. Hypoellipse also calculates the error ellipsoid about the best hypocentral location within which there is 68% confidence that the event occurred. The surface projection of the error ellipsoid for the best location is shown in Fig. 5 (shaded region). Both relative timing of seismic and acoustic phases and acoustic waveform modeling (discussed later) indicate that the summit explosions are located at very shallow depth beneath

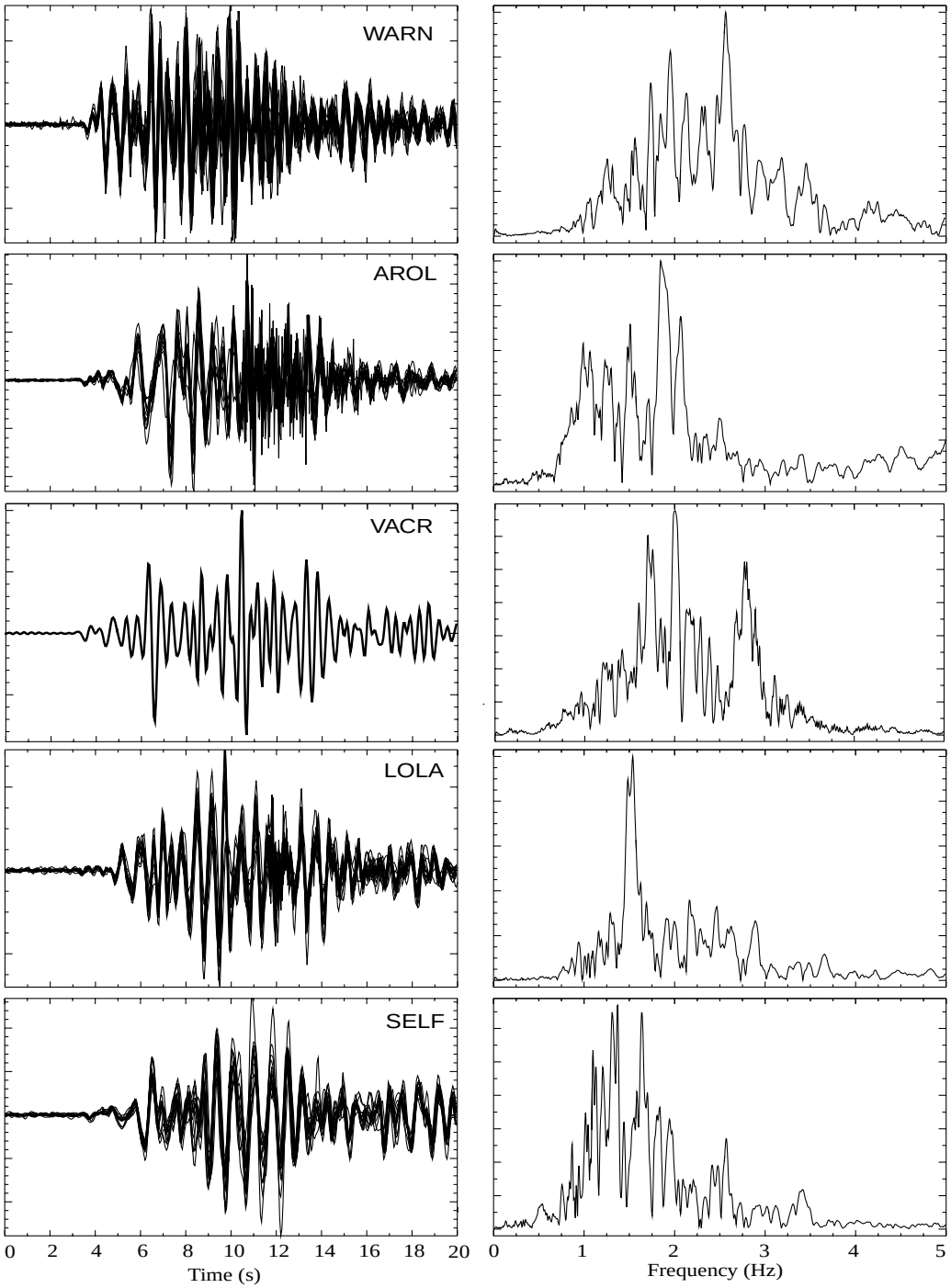

Fig. 4. Explosion waveforms and stacked spectra for 20 events occurring on day 349. Left column: At each site expect VACR, the 20 normalized and aligned waveforms are overlaid. Right column: Stacked (normalized) spectra plotted on a linear-linear scale.

Table 1
Day 349 summit explosion first arrival times measured at each station with respect to arrival times at WARN. The arrival time difference at VACR was determined from an impulsive explosion on day 320 (see text). Avg and std are average and standard deviation times (s), respectively, of each column

Explosion no.	AROL	LOLA	SELF	VACR
3	0.15	0.26	0.39	
5	0.32	0.50	0.46	
10	0.22	0.52	0.51	
11	0.14	0.44	0.39	
14	0.38	0.48	0.44	
15	0.23	0.50	0.42	
16	0.16	0.49	0.36	
17	0.28	0.50	0.52	
18	0.24	0.46	0.40	
19	0.19	0.44	0.39	
20	0.22	0.50	0.37	
21	0.20	0.47	0.40	
22	0.26	0.46	0.35	
24	0.22	0.49	0.45	
27	0.22	0.45	0.41	
28	0.25	0.47	0.37	
29	0.16	0.47	0.37	
30	0.21	0.49	0.41	
31	0.26	0.52	0.49	
32	0.12	0.48	0.71	
33	0.11	0.25	0.46	
Avg ± std	0.22 ± 0.06	0.46 ± 0.07	0.43 ± 0.08	0.35

the active vent and that the seismic and acoustic explosion sources are co-located. In order to determine whether a very shallow source location is consistent with the seismic arrival time data, we calculated travel time residuals versus depth (solid circles in Fig. 5), holding the depth constant at values ranging between the surface and 5 km below sea-level, and allowing the epicenters to locate at any point along the grid shown in Fig. 5. There is a local minimum beneath the summit ($z = -1.65$ km) and a global minimum at 0.5–0.7 km below sea level. The inversion code finds the global minimum; however, the precision of the arrival time picks is not sufficient to distinguish between the two minima. All depths less than about 3 km fit the arrival times equally well within the limits of certainty. We therefore favor the very shallow depth immediately beneath the active vent. Travel time residuals for each of the fixed grid points, at a depth of −1.65 km, are contoured in Fig. 5 and confirm that the epicenter is well resolved and is located within a circle of radius ~0.3 km. The use of P arrivals alone precludes a more precise estimate of the source depth. This is further exacerbated by the fact that our ring of stations are nearly at the same elevation, so that travel times from an event 1 km above the stations are nearly identical to those from an event 1 km below the stations. In addition, the P waveforms are emergent and contain low frequencies within a narrow bandwidth, hence they are difficult to pick with accuracy. These factors all combine to severely limit depth resolution. Unfortunately, they are inherent to volcano seismology studies and cannot be avoided except for the few volcanoes with little topographic relief.

While no clear S phases could be identified in the broadband seismograms, the first arrivals on the transverse components of the temporary array deployment have an apparent phase velocity of about 1.25 km/s and may represent S energy. Under the assumption that the time interval between the first transverse energy and the P onset at WARN ($\delta t = 1.0 \pm 0.3$ s) represents the S–P time, we computed predicted S–P times versus depth for WARN using Hypoellipse and a V_p/V_s ratio of 1.78. The resulting S–P times (triangles

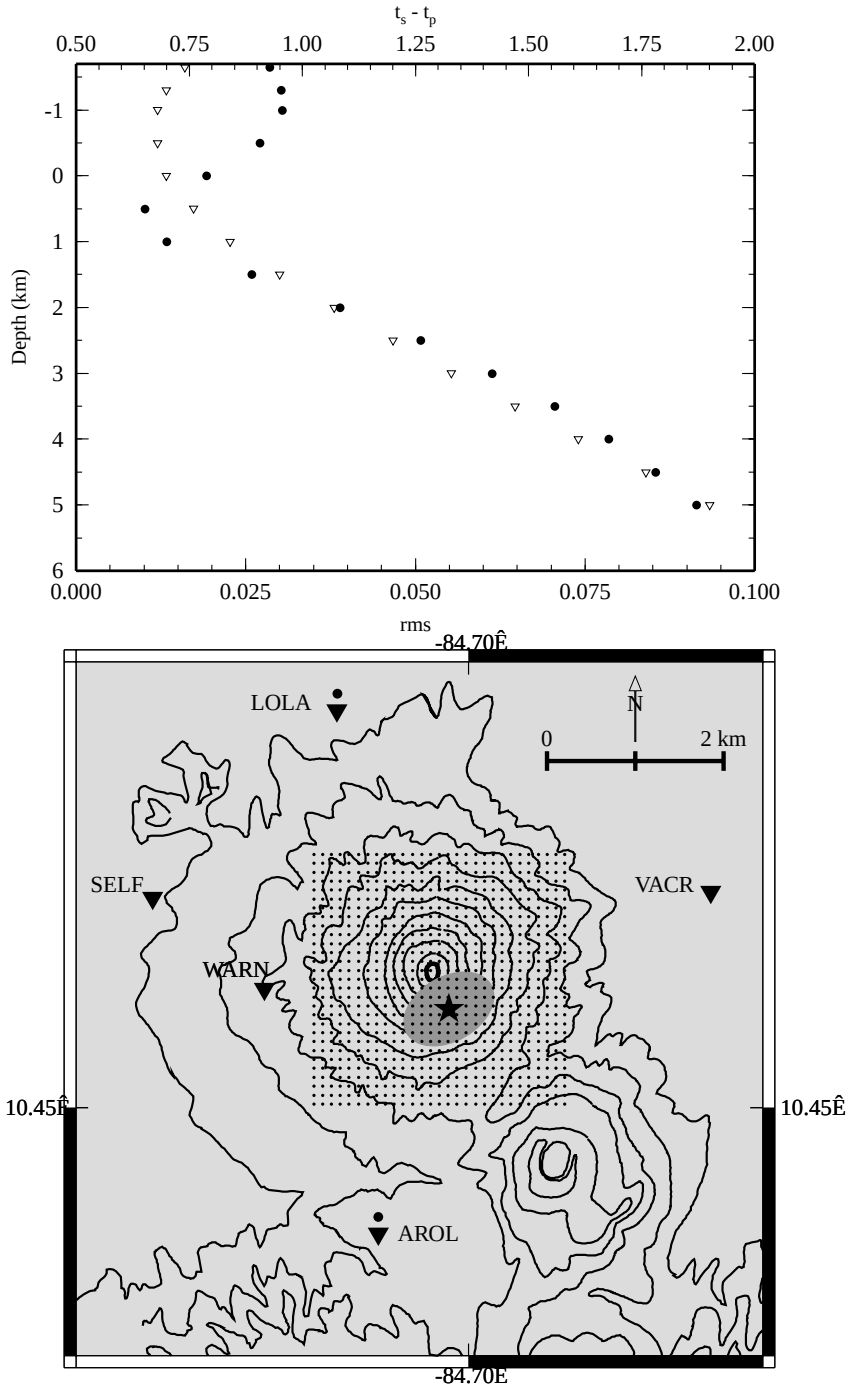

Fig. 5. Top: average travel-time residual ($rms = \sum_{i=1}^{5} \mathrm{resid}_i^2)^{1/2}$) (circles), and predicted S–P time at WARN (inverted triangles) versus depth. The summit is located at −1.65 km. Bottom: contours of rms residual versus epicentral location. The best location is denoted by the star and the shaded region represents the surface projection of the error ellipsoid.

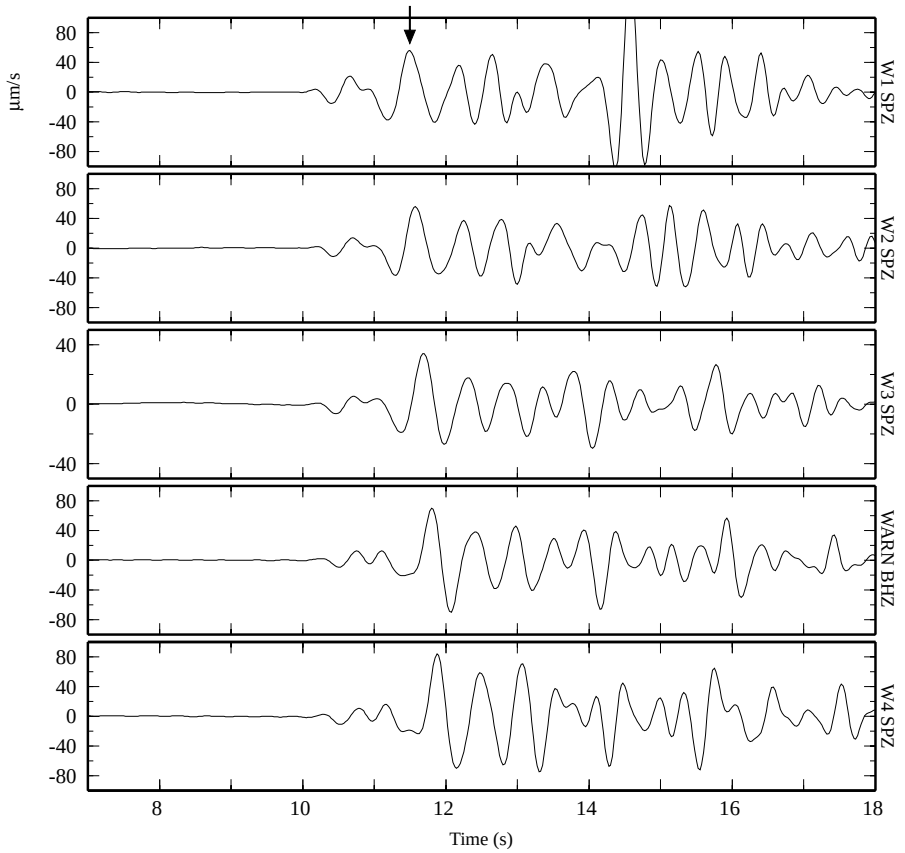

Fig. 6. Low-pass filtered ($f < 3$ Hz) vertical velocities of explosion 122 recorded by the array. A large secondary arrival with a phase velocity of about 1.3 km/s is indicated by the arrow and is most likely SV energy.

in Fig. 5) add a little more constraint on the depth estimate ($h < 2$ km). Further depth constraints come from analysis of air wave arrival times and video recordings and are described below.

4.3. Seismic array phases

Because of the finer element spacing (100 m) of the temporary array, the seismic wavefield is much more coherent and several phases can be identified in the explosion profiles. Several methods exist to measure the apparent azimuth and incidence angles of approaching seismic energy based on the relative arrival times across an array (e.g. f–k beamforming, stacking, etc.). Because our array is linear, we can only measure the apparent slowness along the array axis, or equivalently, the horizontal phase velocity c, across the array. To do this, very small time delays need to be measured over the 100-m station separations. A technique for measuring small time differences between two traces based on the phase of their cross-spectrum has shown promise for estimating relative earthquake locations with great precision (e.g. Frémont and Malone, 1987); however, we found that time-domain cross-correlation methods produce better estimates of time delay and, therefore, slowness for narrowband signals. Fig. 6 shows the low-pass ($f < 3$ Hz) filtered vertical velocities for an explosion recorded by the array. Note the high coherency of the filtered waveforms and the appearance of a large secondary wavetrain (marked with an arrow) that moves out in time with respect to the P onset. In order to determine the phase velocity of the P onset, we computed cross-correlations of all the traces with

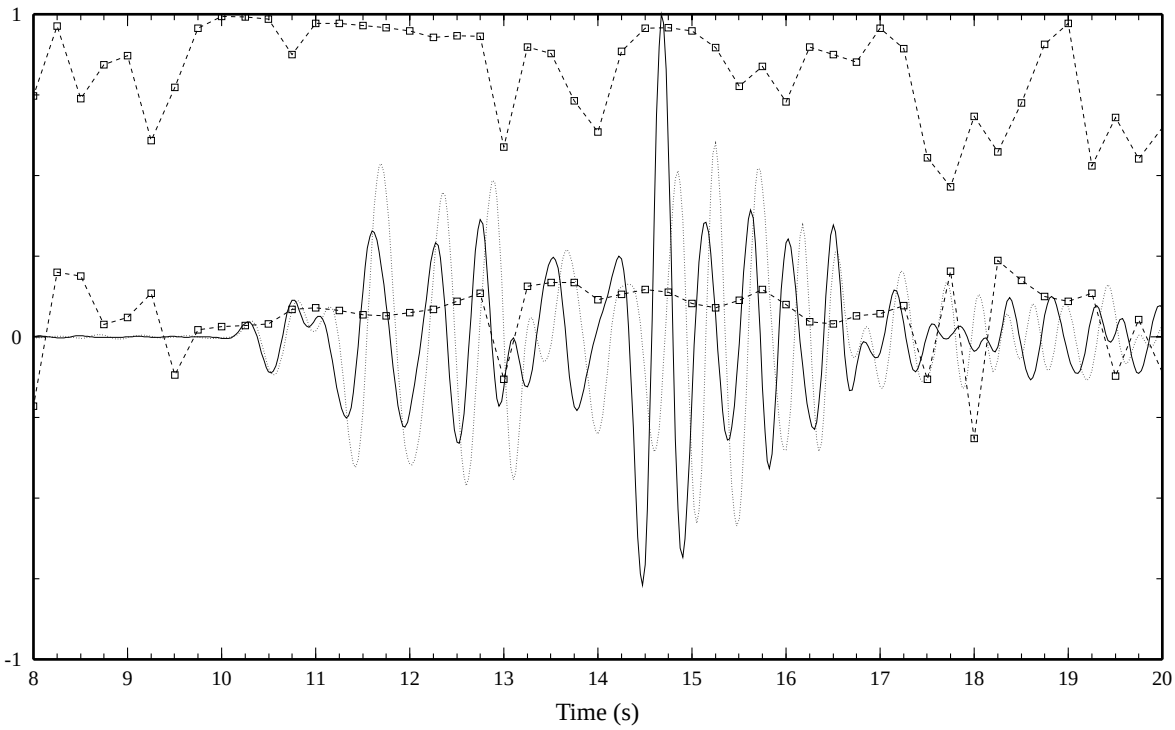

Fig. 7. Running cross-correlation of vertical component velocities for explosion 122 recorded at array stations W1 and W2. The top and bottom dashed traces with squares are the amplitude and delay time, respectively, of the cross-correlation maximum. The solid and dashed waveforms are the normalized vertical velocity traces at W1 and W2, respectively.

respect to station W1. For this case we used a slightly wider Butterworth filter ($f_c = 5$ Hz) to ensure a sharp energy onset, and a small time window (1.85 s) centered on the P onset at each station. The resulting cross-correlation functions show that the initial onset moves out with a phase velocity of 3.3 km/s. In order to obtain a more detailed estimate of the phase velocity of both the P onset and the later phases, we computed the running cross-correlation between stations W1 and W2 using a technique similar to that outlined by Spudich and Cranswick (1984).

The running cross-correlation between two traces is generated by computing the cross-correlation within small windows of data centered about a time t_0 that is shifted forward in incremental steps across the traces. A 50% cosine-squared taper is applied to the data windows prior to computing the cross-correlation in order to isolate the measurements in time. The calculated cross-correlation amplitudes are normalized by the magnitude of the mean auto-correlation within each window. The time offset, τ_m, and the normalized amplitude, $xc_m(\tau_m)$ $(0 \leq xc_m \leq 1)$, of the maximum correlation in each window are output. Because we are attempting to measure very small time shifts between station pairs (e.g. $\Delta t \sim 0.03$ s) with respect to the sampling interval ($\Delta t_s = 0.025$ *s*) and the dominant signal frequency ($f \sim 1.7$ Hz), we found it necessary to first interpolate the traces to a finer sampling interval ($\Delta t_s = 0.003125$ s). Theoretical studies have shown that interpolation prior to cross-correlation can allow accurate measurements of time shifts as small as 1/10 of the original sample interval. We performed several synthetic tests which showed a minimum time shift resolution of about twice the new sampling interval, or $\Delta t \sim 0.0063$ s.

The results for stations W1 and W2 are shown in Fig. 7 for a 1 s computation window, shifted in 0.25 s steps. The top, dashed trace is the amplitude of the cross-correlation maximum, xc_m, as a function of

Table 2
Running cross-correlation (W1, W2 vertical components)

Time (s)	Slowness (s/100 m)	Phase vel. (km/s)
9.500	−0.118750	
9.750	0.021875	4.57
10.000	0.031250	3.20
10.250	0.034375	2.91
10.500	0.040625	2.46
10.750	0.084375	1.19
11.000	0.090625	1.10
11.250	0.081250	1.23
11.500	0.068750	1.45
11.750	0.065625	1.52
12.000	0.075000	1.33
12.250	0.084375	1.19
12.500	0.109375	0.91
12.750	0.134375	0.74
13.000	−0.131250	−0.76
13.250	0.156250	0.64
13.500	0.168750	0.59
13.750	0.168750	0.59
14.000	0.115625	0.86
14.250	0.131250	0.76
14.500	0.146875	0.68
14.750	0.137500	0.73
15.000	0.103125	0.97
15.250	0.090625	1.10

time. Beneath this are the overlaid normalized vertical velocity traces at W1 (solid line) and W2 (dashed line), shown with absolute timing, and on top of these τ_m, the peak cross-correlation offset in seconds, is plotted as a function of time. For perfectly correlated signals, $xc_m = 1$. The cross-correlation amplitude is nearly unity from the P onset ($t = 10$ s) until the end of the low-frequency wavetrain ($t \sim 13$ s). Measurements of τ_m for other station pairs (e.g. W1–W4) yield similar values when scaled to the single inter-station spacing of 100 m. The horizontal phase velocities ($c = 1/(10\ \tau_m)$) as a function of time are listed in Table 2. Measured values of the phase velocity during the first cycle of the P onset range from 2.5–4.6 km/s (Table 2), with 3.0 km/s being a best average estimate for the onset. A similar phase velocity of 3.1 ± 0.1 km/s was measured for P onsets at Pavlof Volcano by McNutt (1986), while Chouet et al. (1997) measured apparent bodywave phase velocities of 1.4–3.0 km/s at Stromboli. McNutt (1986) noted two faint secondary phases in the vertical profiles with phase velocities of 1.04 and 0.53 km/s, respectively. The secondary vertical wavetrain observed in the low-passed profiles (Fig. 6) has a phase velocity of 1.3 ± 0.2 km/s (Table 2). Although polarization and particle motion analyses of this phase were inconclusive, the phase velocity and gross features are consistent with SV energy.

Fig. 8 shows the low-pass filtered north components of velocity for event 122. Though not as coherent as the vertical waveforms, the traces are surprisingly coherent. Because of the east–west orientation of the array, the north component traces form a transverse profile with respect to the summit. A prominent transverse pulse arrives at around 12 s at W1 and can be seen to move out across the array. In order to measure the phase velocity of this arrival we applied the running cross-correlation technique to the transverse waveforms at W1 and W2. The amplitude of the maximum cross-correlation function, xc_m, is not as close to unity as for the vertical waveforms, however, during the large transverse arrival (~12.25–13.75 s) the correlation is significant. The estimated phase velocity of the arrival is 585 ± 55 m/s (Table 3). The slow phase velocity and large transverse amplitude of this phase suggest that it is a Love wave propagating within the shallow unconsolidated layers of the edifice.

4.4. Ground-coupled air waves

Fig. 9 shows normalized vertical velocities and associated spectrograms for three different events recorded at AROL. The top trace is a magnitude 4 earthquake located 75 km SE of Arenal. Most of the P and S wave energy is contained in frequencies above 4 Hz. In contrast, the spectral energy of the summit explosion displayed in the middle trace is concentrated between about 1–3 Hz. In fact, the explosion waveform and its spectrogram look remarkably similar to those of LP earthquakes located 1.4 km beneath Redoubt Volcano, Alaska (Lahr et al., 1994). However the P arrivals observed at Arenal are emergent and do not contain the high-frequency onsets (up to 10 Hz) observed at Redoubt. This may reflect differences in the state of the crater vent between the two volcanoes—closed for Redoubt, open for Arenal. The high-frequency energy (4–8 Hz) arriving at 18 s is the air wave. The bottom trace in Fig. 9

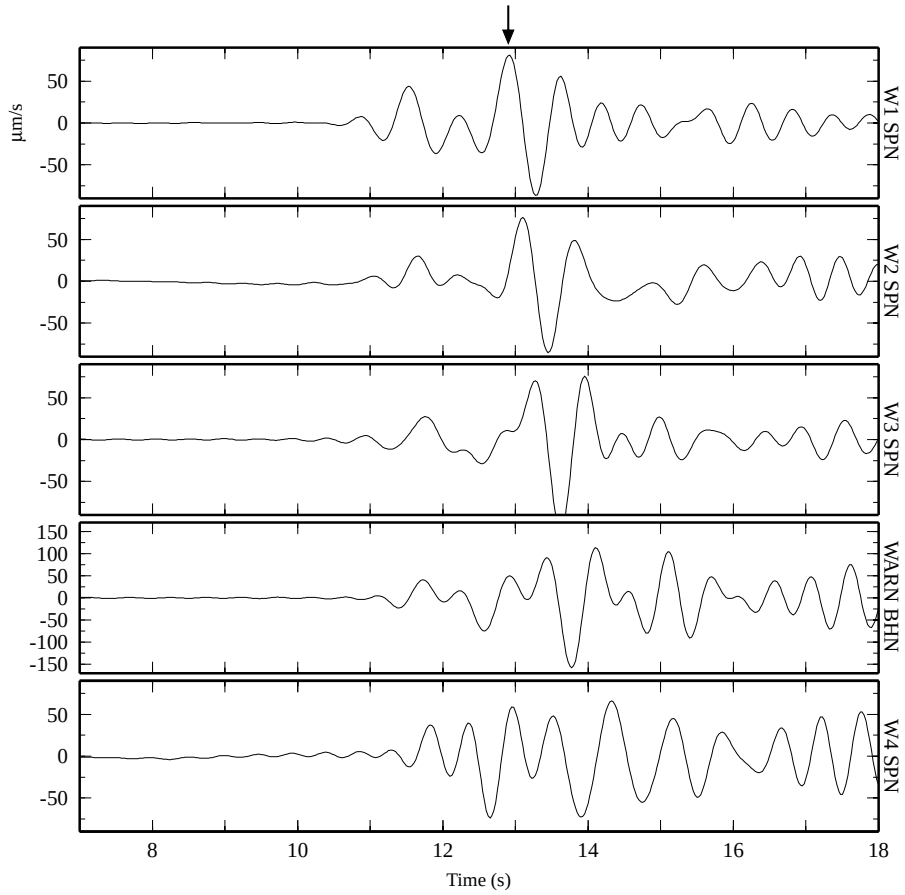

Fig. 8. Low-pass filtered ($f < 2$ Hz) transverse (N) velocities of explosion 122 recorded by the array. A large secondary arrival with a phase velocity of about 585 m/s is indicated by the arrow and is mot likely a Love wave propagating within the shallow layers of the volcanic edifice.

shows a summit explosion on Julian day 332 that produced an energetic air wave. The seismic energy is peaked at ~5 Hz; however this eruption must have emitted significant acoustic energy at much higher frequencies as it was easily audible several kilometers from the summit.

The air wave arrivals move out with the speed of sound in air (~340 m/s). They initially exhibit Rayleigh wave particle motion, however, the wavefield becomes increasingly complex later in time, with significant energy on the transverse component as well. Braun and Ripepe (1993) examined air waves from both natural and artificial explosions at Stromboli and concluded that the air wave propagates at least into the upper 1 m of the ground and sets up local Rayleigh waves in the Z–R plane and Love waves in the N–E plane. The low propagation velocity of the ground-coupled air wave suggests that the airborne acoustic wave pushes on the ground as it descends from the summit vent, setting up a local seismic disturbance rather than exciting a faster propagating wavefield within the ground. The air waves preferentially couple to the higher frequencies (4–7 Hz) of the seismic wavefield, as expected for a layered structure with low-velocity outermost layers; Maximum coupling between the air and the ground occurs for those frequencies whose seismic phase velocities are equal to the speed of sound in air (Press and Ewing, 1951; Press and Oliver, 1955). We are currently investigating the ability of inclined, layered seismic velocity models to produce the observed frequency-dependent coupling.

Table 3
Running cross-correlation (W1, W2 north components)

Time (s)	Slowness (s/100 m)	Phase vel. (km/s)
9.500	0.196875	0.51
9.750	−0.009375	
10.00	0.081250	1.23
10.25	0.134375	0.74
10.50	0.128125	0.78
10.75	0.103125	0.97
11.00	0.084375	1.19
11.25	0.103125	0.97
11.50	0.128125	0.78
11.75	0.118750	0.84
12.00	0.078125	1.28
12.25	0.018750	5.33
12.50	0.187500	0.53
12.75	0.171875	0.58
13.00	0.159375	0.63
13.25	0.159375	0.63
13.50	0.171875	0.58
13.75	0.181250	0.55
14.00	0.156250	0.64
14.25	−0.003125	
14.50	−0.071875	−1.39
14.75	−0.109375	−0.91
15.00	0.256250	0.39
15.25	0.268750	0.37

4.5. Seismic–acoustic partition

The two explosion waveforms shown in Fig. 9 demonstrate the high degree of variability in the seismic efficiency of volcanic explosions. Event 349 (middle panel) contains a relatively sharp seismic onset and a small ground-coupled air wave. In contrast, event 332 (bottom panel) contains an emergent P onset and a large air wave. This illustrates a property observed in the data set: explosions either produce sharp seismic arrivals with relatively impulsive (high signal-to-noise ratio) P onsets and small air waves or emergent (low signal-to-noise) P onsets with large air waves. Mori et al. (1989) observed a similar relationship between the relative amplitudes of the seismic and acoustic waves for summit explosions at Langila Volcano. The difference in explosion energy partitioning between the seismic and acoustic wavefields could reflect a changing source depth, with deeper explosions coupling more efficiently into the ground. In order to determine whether the explosion source depths are changing with time, we examined the time difference between the seismic onset (P) and the ground-coupled air wave (A) for several explosions. Regardless of whether the seismic and acoustic explosive sources are co-located, if either one were changing location appreciably from eruption to eruption, the time difference between P and A, $\Delta t_{AP} = t_A - t_P$, should vary. In order to precisely measure Δt_{AP}, we first align the broadband traces with respect to the P onset of the master event (95:349) at each station. The event trace is then high-pass filtered to reveal the air wave, and the timing of the air wave with respect to the P onset is measured. This procedure was performed for several events recorded at the broadband stations. Fig. 10 shows high-pass filtered seismic recordings of the air wave at AROL for several explosions with varying air wave amplitudes, plotted on a common scale, and aligned so that the P onsets, visible in the broadband traces, appear at $t =$ 10 s. While the ratio of P to air wave amplitude varies for the different events, the timing between the two phases is stationary. Because of the short time scales (less than a minute) over which the seismic-acoustic partition varies, and because of the short propagation distance ($<$2 km) of the acoustic waves, it is unlikely that the acoustic amplitudes, and therefore the seismic–acoustic partition, are affected by changing atmospheric conditions; in fact, during our array experiment we observed highly variable seismic–acoustic partitioning during periods of clear skies without wind.

Alternatively, the energy partitioning may be governed by the degree of openness of the explosion vent and/or the coupling efficiency between the seismic and acoustic wavefields which depends on the gas flow properties and the boundary conditions (Garcés and Hansen, 1998). Small changes in the gas concentration of the magma–gas mix within the conduit will produce large changes in the acoustic velocity (Kieffer and Sturtevant, 1984), greatly affecting the acoustic impedance (ρc) of the magma. An explosion detonated in a high void fraction, low sound speed, low density magma–gas mixture would preferentially couple into the atmosphere because the magma impedance is better matched to the impedance of the atmosphere than to the impedance of the solid rock (Garcés et al., 1998). Even when large changes in Δt_{AP} are reliably measured for volcanic explosions, it may be more reasonable to attribute them to small changes in

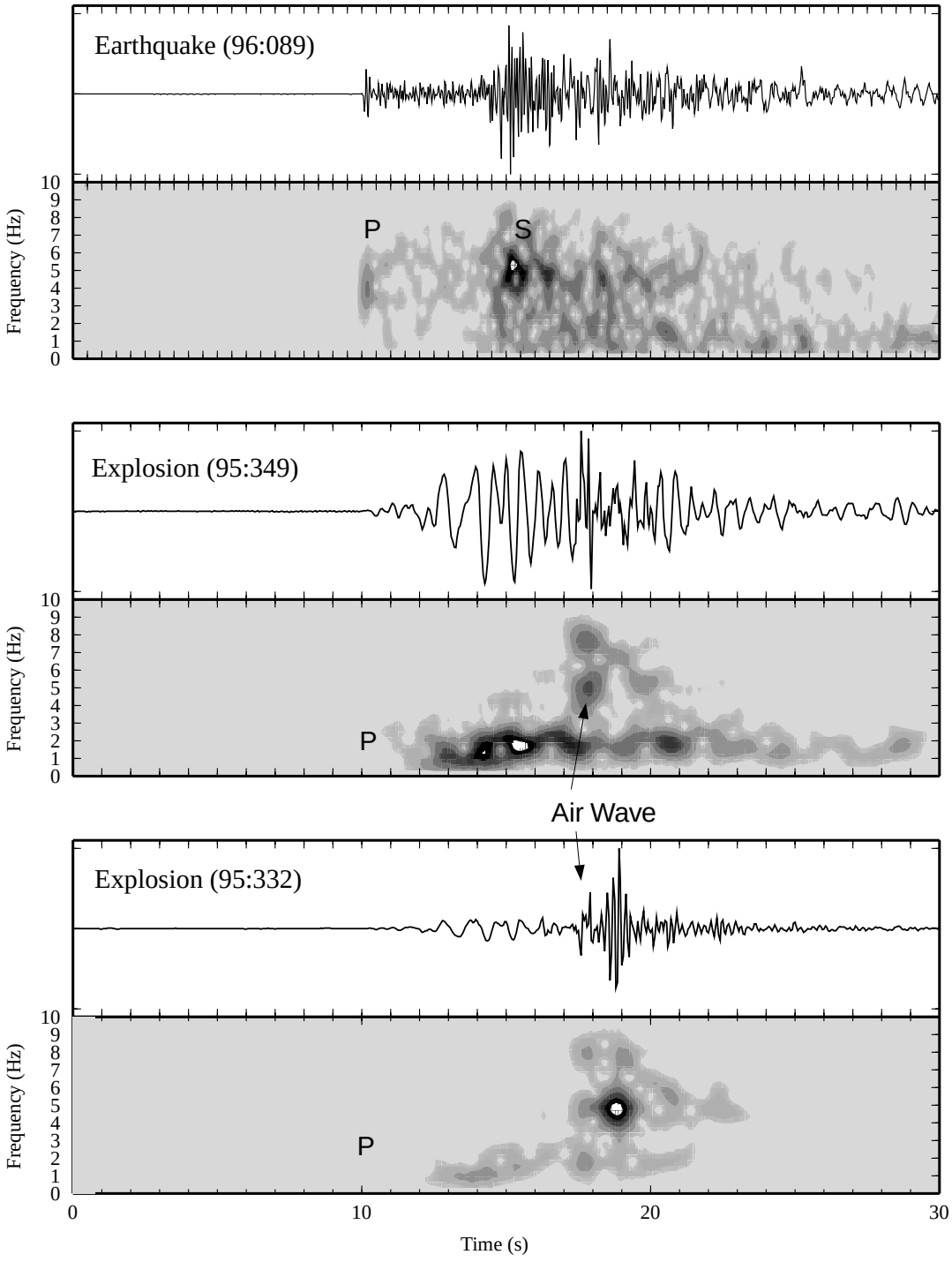

Fig. 9. Three seismic events and their corresponding spectrograms recorded at AROL. Top: a magnitude 4.0 earthquake located 75 km SE of Arenal. Middle: summit explosion (day 349 master event). Bottom: summit explosion from day 332.

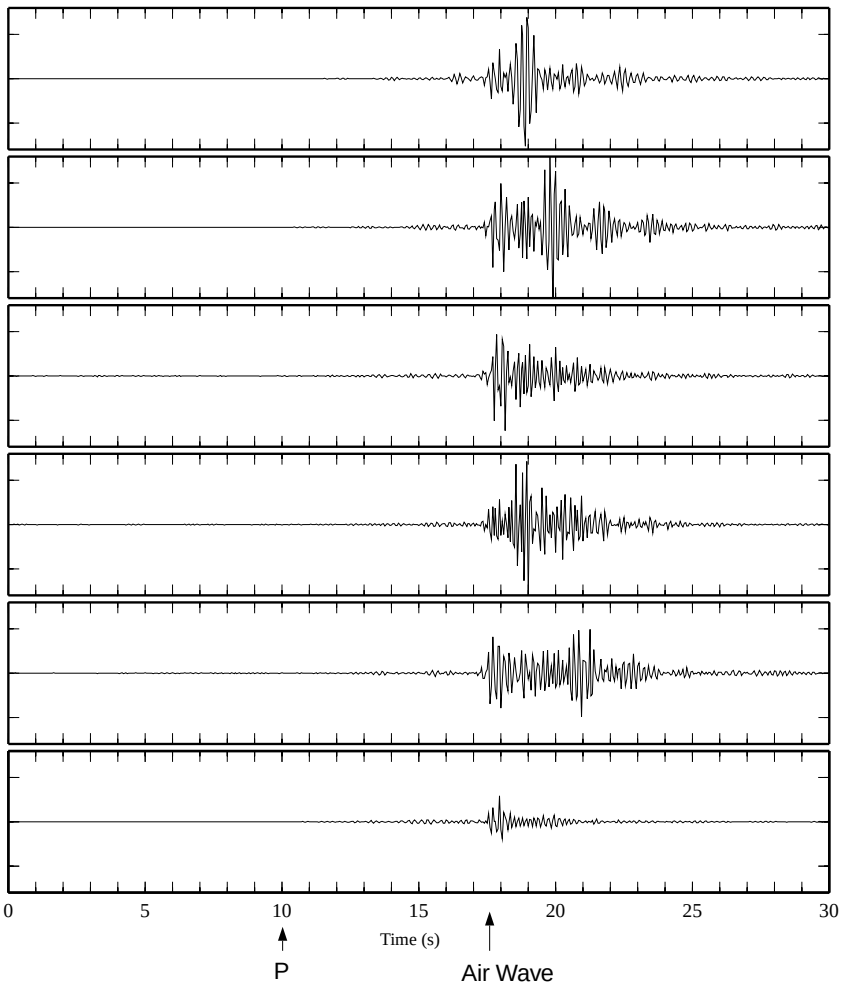

Fig. 10. High-pass filtered vertical velocities for several explosions recorded at AROL. Traces are plotted on a common amplitude scale and are aligned so that the P onsets, which are aligned with the master event and are not visible in the high-passed traces, arrive at $t = 10$ s. Note that the timing between the P onset and the air wave is constant for the different events.

the gas concentration of the conduit, which exert strong influence on the acoustic velocity, than to large depth variations over small time scales. Similarly, the observed gliding of harmonic tremor frequencies is more easily modeled with a time-varying gas void fraction than by invoking rapid changes in the length of a resonant conduit (Garcés et al., 2000).

4.6. Explosion depths revisited

In addition to demonstrating the stability of the explosion depth, the time difference between the acoustic and seismic arrivals can be used to determine whether the acoustic and seismic sources are coincident in space and time. Very precise measurements of Δt_{AP} were made at both the broadband sites and the temporary array sites following the procedure described above. In addition, for the temporary array, the air wave arrivals could also be measured directly from the acoustic pressure recordings for the sites equipped with microphones. The source model illustrated in Fig. 11 can be generalized to describe any disturbance (e.g. an injection event) at depth h which radiates the first seismic waves (P onset) to arrive at a

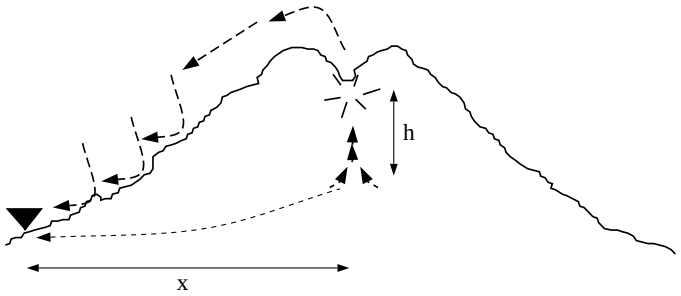

Fig. 11. Schematic source model where an injected magmatic parcel at depth *h* radiates low frequency seismic waves and ascends to shallow depth beneath the vent where it explodes and radiates broadband seismic and acoustic (air) waves. In this model the time difference between the first acoustic and seismic arrivals is a function of the source depth.

station, *x* km away. The disturbance then ascends from depth *h* to the surface vent where it explodes, radiating acoustic waves (A) into the atmosphere. For this model, the time difference between the first acoustic and seismic arrivals is directly related to the source depth *h*:

$$\Delta t_{AP} = \frac{h}{V_h} + \frac{R_A}{V_A} - \frac{R_P}{\alpha} \quad (1)$$

where h is the source depth, V_h is the ascent velocity of the disturbance, and R_A, V_A and R_P, α are the acoustic and seismic slant ranges and velocities, respectively. For large distances ($x \gg h$), the slant range is approximately equal to the distance x. Eq. (1) then simplifies to:

$$\Delta t_{AP} = \frac{h}{V_h} + \left[\frac{1}{V_A} - \frac{1}{\alpha}\right]x \quad (2)$$

With $V_A = 340$ m/s and using reasonable estimates of α, the ratio h/V_h can be estimated at a particular distance x, from the difference between observed Δt_{AP} and that calculated from $[1/V_A - 1/\alpha]x$. This ratio can then be converted into a source depth by assuming an ascent velocity V_h, the value of which will depend on how one assumes the disturbance at h is propagated to the surface. Chouet et al. (1997) found that the measured value of Δt_{AP} was 0.2–0.4 s greater at $x =$ 150 m than predicted by a coincident seismic and acoustic explosive source at the vent of Stromboli. They accounted for the additional time by the time it takes for a rising gas slug, presumed to radiate the onset seismic energy from a depth of 5–15 m beneath the magma surface, to ascend the final meters of the conduit with an ascent velocity of 2–10 m/s (Vergniolle and Brandeis, 1996), before exploding at the surface and radiating the acoustic waves. Alternatively, the disturbance could ascend as a pressure wave, with a much higher compressional velocity, which triggers the detonation of a high-pressure gas pocket just beneath the vent. Such a model has been proposed for Sakurajima volcano, where explosion-quakes at 1–2 km depth are believed to trigger explosive eruptions at shallow depths beneath the crater (Ishihara, 1985).

Fig. 12 shows the measured values of Δt_{AP} as a function of distance from the summit. The values plotted at each site are averages of several measurements at that site, while the error bars (~0.5–1.0 s) are conservative estimates of the scatter at each site and are probably too large. Eq. (2) is the equation of a line, $y(x) = y_0 + mx$, with slope $m = [1/V_A - 1/\alpha]$ and y intercept $y_0 = h/V_h$. In Fig. 12, lines are shown for several different values of compressional velocity α. The maximum value of α (3 km/s) is equal to the phase velocity measured for the seismic onset by the array. The measured phase velocity represents a maximum estimate of the compressional speed, the two being equal only when the seismic energy impinges horizontally on the array (end-fire). The smallest value of α (1 km/s) is taken to be a minimal value of the compressional velocity derived under the assumption of a coincident P and Love wave source region for the large transverse pulse measured by the array. The phase velocity of this pulse ($c \sim$ 600 m/s) is related to the shear velocity by $\beta = 1.1c$ which can then be related to the compressional velocity under the assumption of a Poisson solid ($\alpha = \sqrt{3}\beta = 1.1$ km/s).

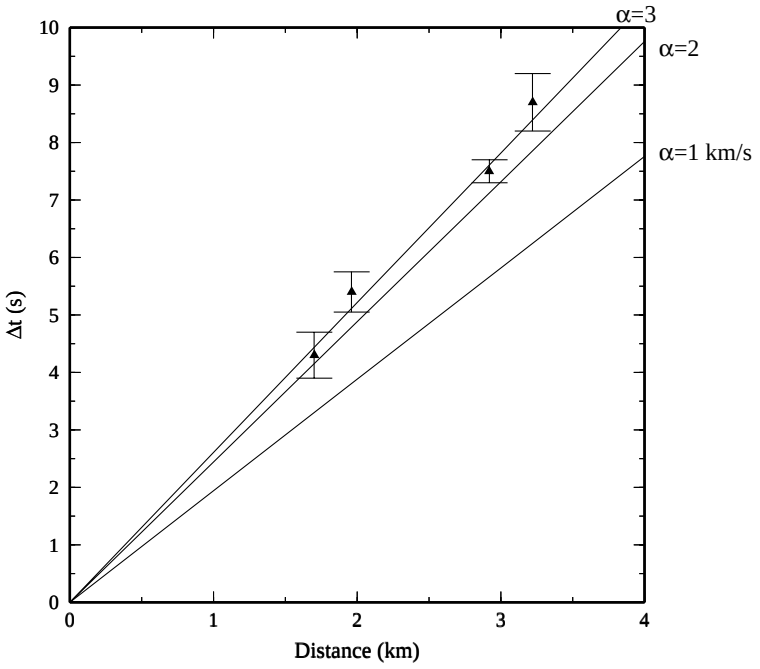

Fig. 12. Predicted (lines) and observed (triangles) time differences between the first arriving acoustic and seismic arrivals (Δt_{AP}) versus distance. Predictions are computed for seismic compressional velocities of 1, 2, and 3 km/s, while observations are averages of many time differences measured at each of four different sites. The slope of the observations is best matched by the higher seismic velocities and the good fit between measurement and prediction allows little depth separation between the seismic and acoustic sources.

Essentially, the lower the value chosen for the seismic velocity, the greater the excess time between measured and predicted Δt_{AP} that can be attributed to source depth h. However, as can be seen in Fig. 12, the steeper lines, corresponding to the higher seismic velocity ($\alpha = 3$ km/s) match the slope of the measured data better than the lines corresponding to lower seismic velocities. A non-zero y-intercept ($y_0 = h/V_h$) will offset the lines vertically but will not change their slopes. Furthermore, for $a = 1$ km/s, an incidence angle of 20° would be necessary to produce a phase velocity of 3 km/s, corresponding to a source depth of 5.5 km, which is incompatible with the P wave arrival times. The correspondence between the seismic phase velocity observed by the array ($c =$ 3.0 km/s) and the compressional velocity of the medium ($\alpha = 2 - 3$ km/s) suggests that the initial seismic energy impinges at low angle to the array axis (endfire) rather than at steep incidence from below. The good match between the predicted and observed times also leaves little room for appreciable depth separation h, between the source of the seismic onset and the air wave. In fact, there is no reason to reject a coincident source at the vent based on the data shown in Fig. 12. At most, the additional time incurred propagating from depth h, is on the order of half a second. If we assume the slug model of Chouet et al. (1997), with an ascent velocity of ~2–10 m/s, then this corresponds to a depth $h = 1 - 5$ m.

An additional piece of evidence in support of a shallow source depth comes from video recordings of summit explosions. A black plume is seen to emerge from the vent approximately 6.8–8.2 s before the arrival of the acoustic wave at AROL. Since it takes the acoustic wave about 9 s to travel from the summit to AROL (assuming $V_A = 340$ m/s), this leaves about 0.8–2.2 s for the plume to ascend the conduit, assuming the explosion simultaneously generated the air wave and the plume. For plume rise velocities of 20–40 m/s (Weill et al., 1992), the corresponding explosion depths are 10–100 m beneath the summit.

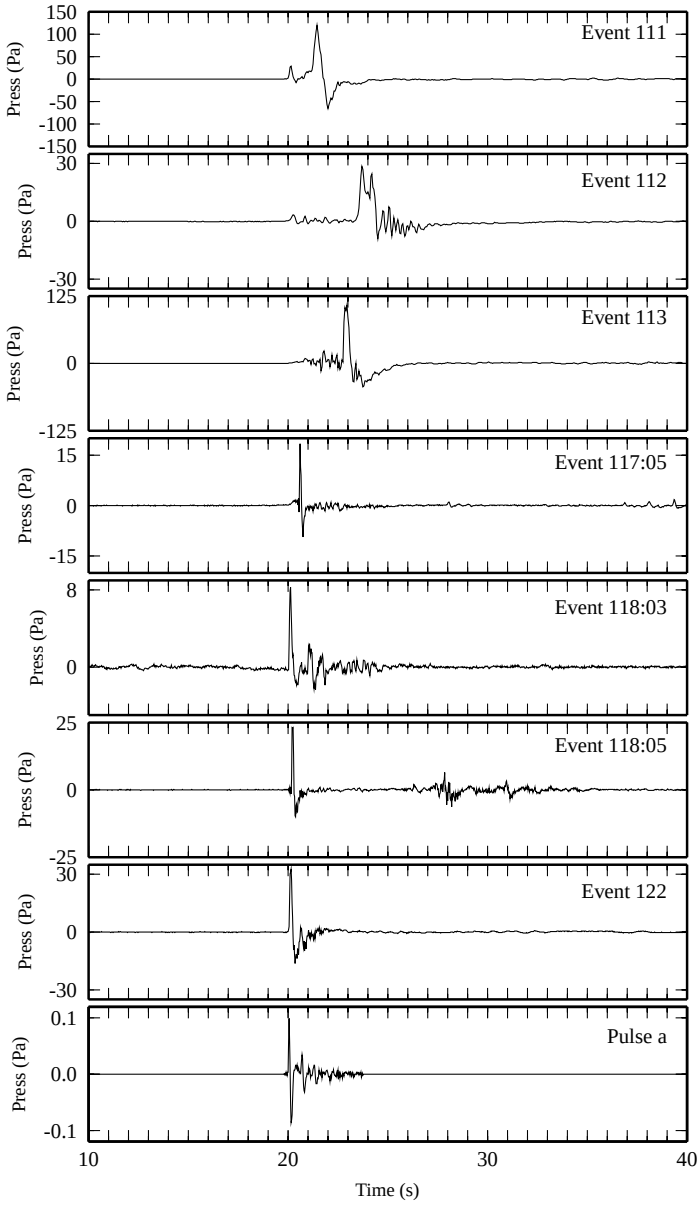

Fig. 13. Acoustic explosion waveforms recorded by the microbarometer. The microbarometer was located at site WARN until 118:16 GMT when it was moved to site W2 to form the radial array.

4.7. Acoustic explosion waveforms

Our seismic observations of large ground-coupled air waves motivated us to record the explosion pressure waves directly in the air. Acoustic waves generated by explosions travel through a much simpler medium (the air) than seismic waves, and therefore provide a less obstructed view of the explosion process. Fig. 13 shows the airborne acoustic pressure waveforms for several explosions recorded by the microbarometer. The explosion waveforms are very simple and begin with a sharp compression followed

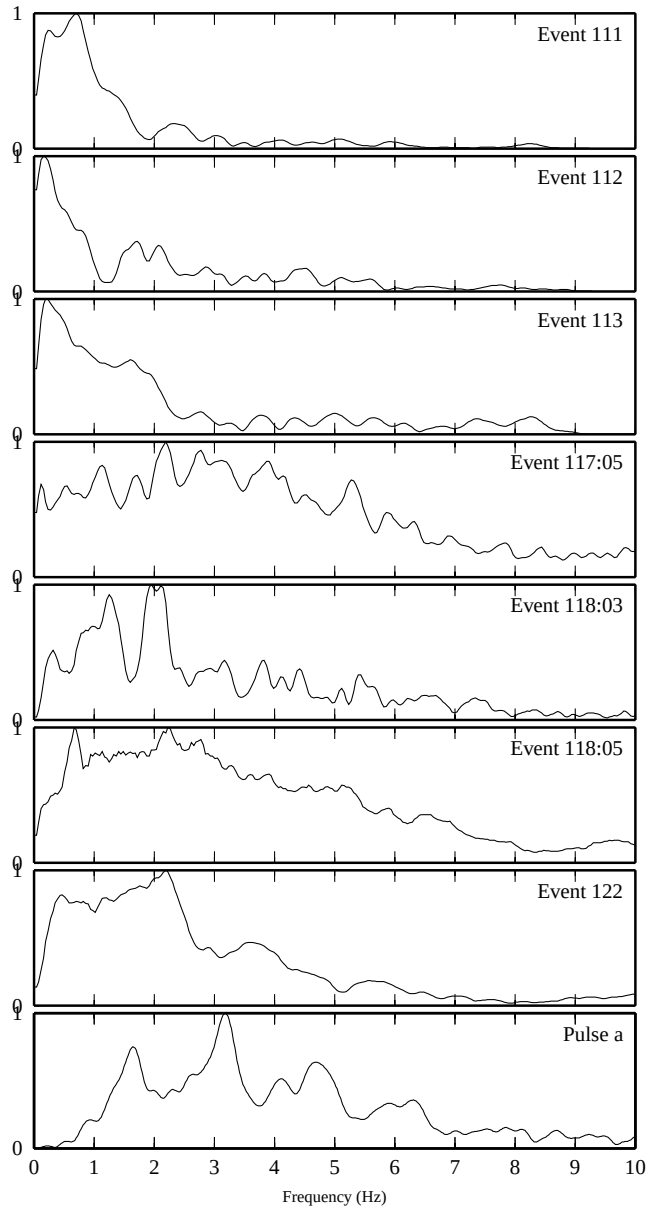

Fig. 14. Normalized Fourier amplitude spectra for the waveforms shown in Fig. 13 plotted on a linear-linear scale.

by a more gradual expansion towards zero pressure. The acoustic amplitudes of the explosions span over three orders of magnitude while maintaining their simple pulse-like waveform. The maximum pressures recorded during this period (~125 Pa at 2 km from the summit) can be compared to those at Stromboli (~50 Pa at 250 m (Vergniolle and Brandeis, 1996)) and Sakurajima (~400 Pa at 2.7 km (Ishihara, 1985)).

The normalized Fourier amplitude spectra for each of the explosions in Fig. 13 are plotted in Fig. 14. The spectra show great variety, though in general, they contain corner frequencies of 0.3–3.0 Hz. Nearly all of the acoustic energy of the Arenal explosions is in

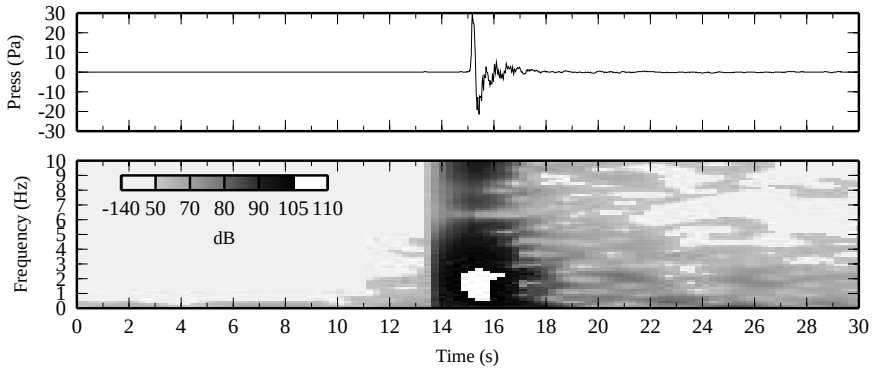

Fig. 15. Top: Acoustic waveform for explosion 122 recorded at WARN. Bottom: Corresponding spectrogram ($dB = 20 \log P/P_0$, $P_0 = 20$ μPa).

the infrasonic range. There is some indication of a decrease in corner frequency with increasing explosion amplitude for the events shown in Fig. 14; this can be seen in particular for two of the smoothest waveforms (events 122 and 111). Above the corner frequency, the spectra show several smaller peaks. These are especially clear for the larger explosions (Events 111, 112, 113) which likely excited the conduit into resonance. The variation of peak frequencies for the different events may reflect different conditions within the conduit, particularly gas concentration.

Fig. 15 shows the acoustic waveform for event 122 along with its spectrogram, showing the sound pressure level (dB) of the waveform in different frequency bands as a function of time. Spectra were computed in 2 s triangular data windows, shifted in 0.25 s steps. The energy of the first few cycles ($t = 15 - 18$ s) is very concentrated in frequencies between 1 and 3 Hz. There is very little evidence for energy before this time, and energy after the main event ($t > 18$ s) is not concentrated within any particular frequency band. Because the acoustic waveforms recorded at Arenal are very similar to those recorded at Stromboli by Vergniolle and Brandeis (1996), it is instructive to compare our findings with theirs. Vergniolle and Brandeis (1996) analyzed acoustic waveforms of 36 Stromboli explosions using the same model B&K microphones we used at Arenal, positioned 250 m from the active east vents. The recorded waveforms at Stromboli look very similar to our recordings at Arenal, though the amplitudes are smaller (<50 Pa at 250 m, with 5 Pa more typical) as are the pulse half-durations (~0.06 s). They divided the acoustic waveforms into three parts: (1) the period before the sharp rise in amplitude (main event); (2) the main event; and (3) the period after the main event. They found that the first part contains primarily 2 Hz energy, which approximately doubles in power during the 30 s preceding the main event. The second part constitutes the main event and contains a broadband frequency spectrum, with peak intensities ~130 dB centered at about 9 Hz and a second frequency peak at 4.5 Hz. The third part begins just after the main event and is characterized by the appearance of higher frequencies (1–10 Hz), particularly at 4.5 Hz. Vergniolle and Brandeis (1996) explain their observations in terms of a model of slug flow, where gas pockets which form at depth by coalescence of a foam layer are overpressurized by the release of surface tension from numerous small bubbles. The overpressurized, meter-sized bubble then ascends the magma conduit with a rise velocity of ~1.6 m/s (Wallis, 1969) towards the vent. The acoustic energy emitted during part 1 is hypothesized to be produced by longitudinal oscillations of the nose of the rising bubble during the last 30 m of ascent. The main event (part 2) is believed to represent volumetric oscillations of the bubble just beneath the magma–air interface before the bubble bursts. They found that for a bubble radius of ~0.5–2 m, bubble lengths from a few meters to a few tens of meters could explain the predominant 4–10 Hz frequencies of the main event. The higher frequencies of part 3 are believed to be caused by

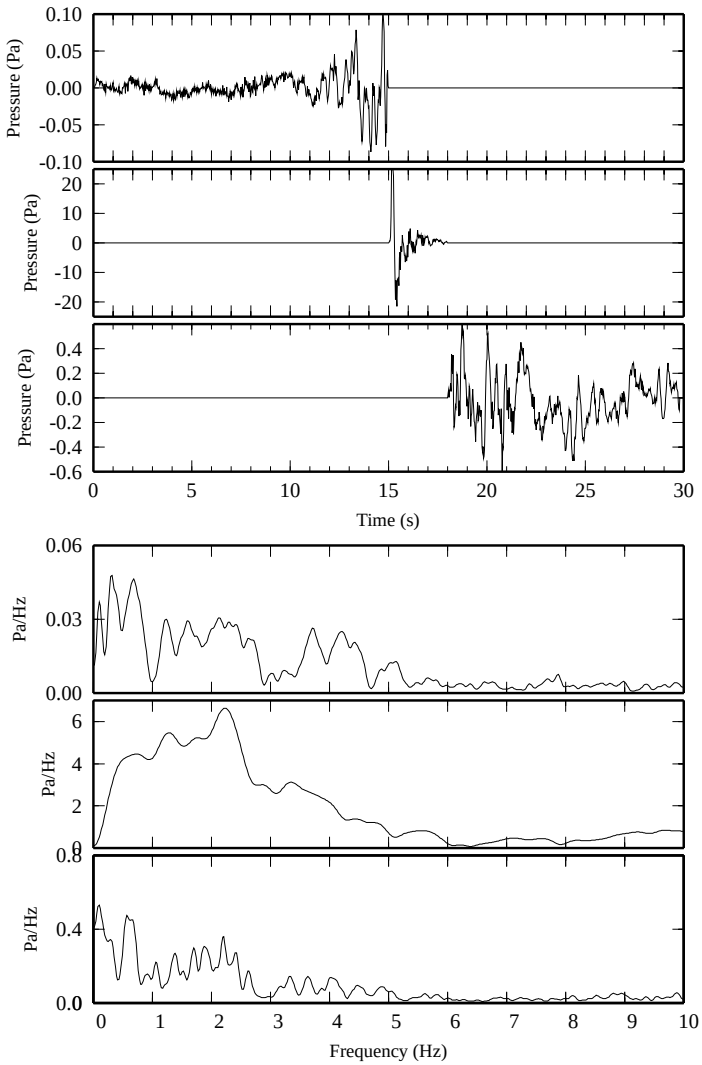

Fig. 16. Top three panels: Acoustic waveform for explosion 122 divided into three time periods before (top), during (middle) and after (bottom) the main explosion. Amplitudes are given in Passcals. Bottom three panels: Corresponding Fourier amplitude spectra for the three periods. Note significant precursory energy in the first time period.

'kinematic' waves of the lateral film thickness left behind after the bubble bursts.

Fig. 16 shows the division of the acoustic waveform for event 122 into 3 parts—before, during, and after the main event—plotted on different scales. At these enlarged scales, there does seem to be precursory energy prior to the main event. Also shown in Fig. 16 is the corresponding Fourier amplitude spectrum for each window. The longer periods ($f < 1$ Hz) are probably not reliable for the low amplitude pre-event and post-event spectra, given the large amplitude of environmental infrasonic noise at these periods, however the energy between 1 and 3 Hz is significant. Comparison with the other condenser microphone (W1) confirms that the precursory energy is present in both microphones and is propagating with the acoustic velocity (~340 m/s). The higher acoustic frequencies, which are distributed between 2.5 and

Table 4
VOLAR model parameters for event 122

Conduit cross-section area	20 m^2
Length of shallow section (1)	15 m
Density (1)	1×10^3 kg/m^3
Magma sound speed (1)	136 m/s
Dynamic viscosity (1)	1×10^4 Pa s
Relaxation time (1)	1×10^{-3} s
Density of adjacent deeper melt (2)	2×10^3 *kg/m*^{3}
Impedance ratio	$z_{21} = 4.6$
Explosion source pressure	3.4 Mpa
Explosion source corner frequency	0.6 Hz
Explosion source depth	12 m

9 Hz, radiate coincidentally with the main explosion pulse, rather than after the main event, as might be expected for post-explosion jetting. It is possible that the first arrivals of the more complex acoustic events (111, 112, and 113), are themselves precursors to the subsequent larger events, however, there does not appear to be a stationary scaling between these "priming triggers" and the subsequent main events. Thus, while we do possibly detect precursory energy, implying system priming prior to large explosions, we do not observe a lower precursor frequency content, or any evidence of a different acoustic source mechanism operating. The acoustic pulse is observed to decay as $1/r$, suggesting a strong monopole source component (Lighthill, 1978). Monopole radiation also provides a consistent mechanism for the observed mass flux during strombolian eruptions.

4.8. Acoustic explosion modeling

Several issues must be addressed before seismic and acoustic recordings can be utilized to constrain volcanic source processes. For the seismic recordings in particular, propagation through a heterogeneous structure of great topographic relief produces considerable effects on the resulting waveforms. Utilization of the seismic waveforms to characterize the source requires improved understanding of these effects. However, the propagation of acoustic waves through the atmosphere presents a much simpler problem, hence, we concentrate on modeling the explosion acoustic waveforms first, with the goal of later combining the resulting acoustic source model with models of seismic excitation and propagation. In this section we present preliminary efforts to model the strombolian explosions at Arenal using the Volcano Acoustic Resonance (VOLAR) model (Buckingham and Garcés, 1996; Garcés and McNutt, 1997). The VOLAR model predicts the airborne sound field radiated by a magmatic conduit that is excited into resonance. The source function is determined either by specifying an explosive point source in the magma column or by specifying either the pressure or velocity at one of the ends of the conduit. The conduit is modeled as a series of magma–gas filled sections with the cross-sectional area, length, density, sound speed and viscosity specified within each section. The conduit is embedded in a solid half-space, while the atmosphere is treated as a fluid half-space connected to the conduit at the vent opening. The vent is modeled as a pressure-release surface for energy incident from below. Further details of the model can be found in Garcés and McNutt (1997). The VOLAR model was run iteratively with conduit parameters adjusted to best match the acoustic waveform for event 122. The observed and predicted waveforms for this event are plotted in Fig. 17. The match is good, including the secondary reflection pulses that follow the main pulse. The corresponding model parameters for a two layer conduit are listed in Table 4. We must stress that they are not unique, and different parameter combinations corresponding to different scalings of the model can be found to match the data. However, the parameter values listed in Table 4 are reasonable estimates and are compatible with theoretical and experimental estimates of magma parameters (e.g. Murase and McBirney, 1973). Of particular interest are the explosive source depth, the shallow magma–gas sound speed, and the impedance ratio between the shallow and deep sections of the conduit. These parameters must be chosen together to match both the timing and the amplitude of the secondary pulses. These pulses represent energy reflected downward from the vent and upward from the boundary between the shallow and deep sections of the conduit. The shallow explosion depth ($h =$ 12 m), is consistent with estimated explosion depths at Stromboli [$h < 100$ m, Chouet et al. (1997)]. The large pressure gradients which are predicted by theoretical models of degassing to exist at shallow depths (Sparks, 1997), may provide a region where

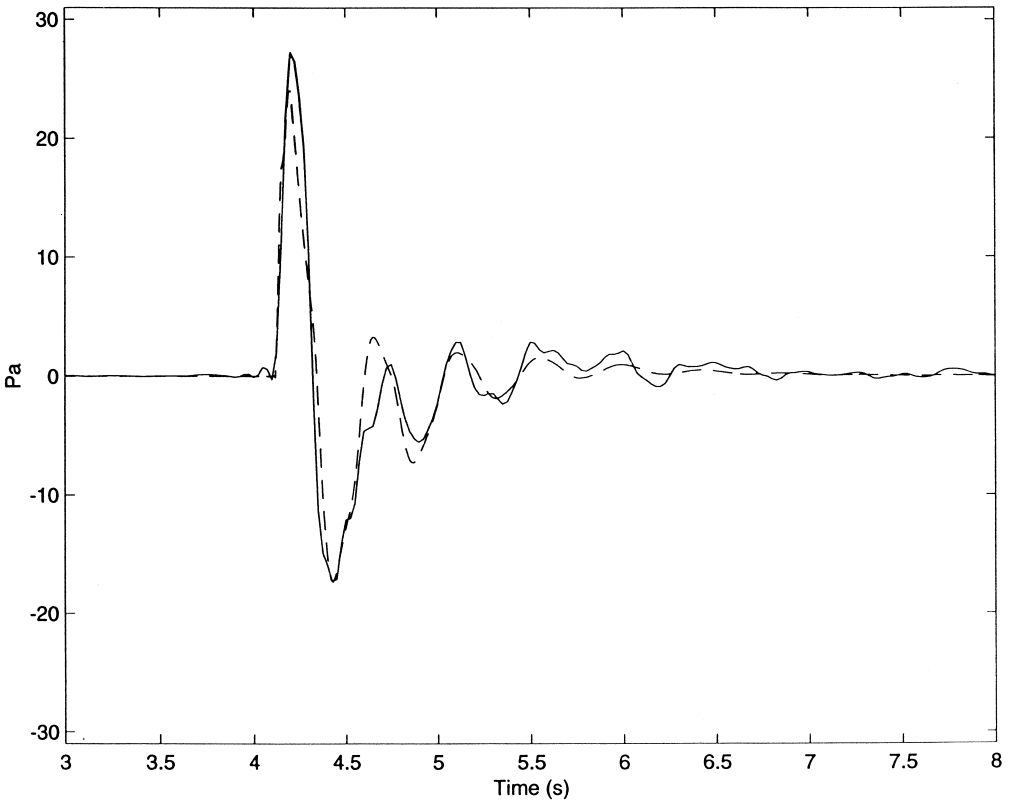

Fig. 17. Synthetic (dashed line) and observed (solid) acoustic waveforms for event 122. The synthetic waveform was generated using the VOLAR parameters listed in Table 4.

violent gas expansion occurs. This model is preliminary; the acoustic waveforms cannot uniquely determine the large number of model parameters and extensive forward modeling must be performed in order to quantify the resolution of each parameter and to understand the parameter interdependences.

5. Harmonic tremor

5.1. Tremor frequency content

Perhaps the seismic signal most strongly identified with volcanoes is volcanic tremor. Volcanic tremor was first observed in 1935 by Sassa at Aso volcano in Japan (Sassa, 1935). Since then some 1100 cases of volcanic tremor have been reported for over 84 volcanoes worldwide (McNutt, 1989). The harmonic tremor seen at Arenal is clearly not a site effect as there is no variation in the harmonic frequencies at the five sites, nor on the three components of any site (Hagerty et al., 1997). Fig. 18 shows normalized velocity spectra for four different, non-consecutive 30 s time periods extracted from the data set. For each time period the spectra for the vertical components at station WARN (thick line) and station LOLA (thin line) are plotted on a log amplitude scale. The top row shows harmonic spectra with a fundamental frequency around 0.9 Hz and both even and odd harmonics. These spectra could be modeled by a simple organ pipe resonator with both ends open. By assuming a value for the acoustic velocity of the resonating medium (c), a scale length (L) for the resonator can then be derived from the fundamental frequency ($f = c/2L$). For instance, for an acoustic velocity of 900 m/s, $L = 500$ m. In the second row the fundamental frequency is slightly increased and the relative amplitudes of the overtones are more

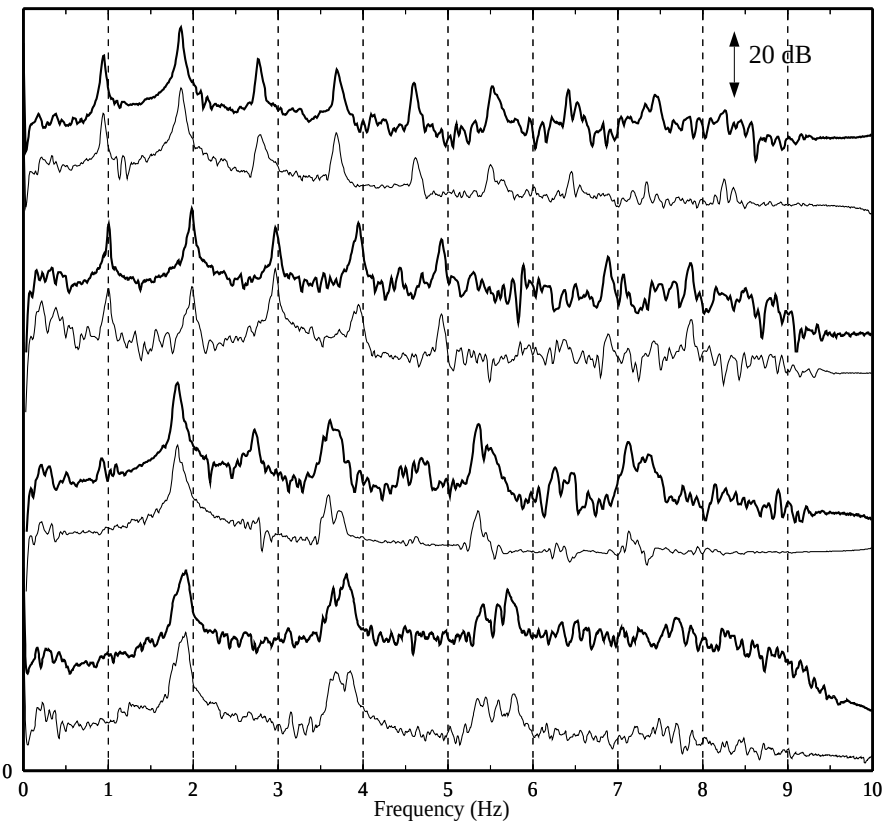

Fig. 18. Normalized log spectral density plots for four isolated, non-continuous 30 s tremor slices recorded at WARN (thick line) and LOLA (thin line). The spectra for different time slices vary considerably but are nearly identical at the two stations.

balanced. In the third row the odd harmonics (0.9, 2.7, 4.5, and 6.3 Hz) are diminished relative to the even. A similar observation was reported for harmonic tremor at Mt. Semeru, Indonesia. Although for this case the even harmonic amplitudes were reported to be systematically lower than the odd (Schlindwein et al., 1995), the difference exists in terminology—they referred to the fundamental as f_0, so that the even harmonics (f_2, f_4), etc.) were found to be reduced (Schlindwein, personal communication, 1996). In the above terminology, where f_1 refers to the fundamental frequency, both volcanoes show a systematic reduction of the odd harmonic peaks (f_1, f_3, f_5, etc.). In the fourth row the odd harmonic peaks are below the noise level, perhaps indicating a closed boundary condition. However, closing one end of the resonator should shift the fundamental frequency to half the open pipe value, and only the odd harmonics (0.45, 1.35, 2.25 Hz, etc.) should be present. Alternatively, if the peak near 1.9 Hz in the bottom pair of spectra is assumed to be the open pipe fundamental mode, the corresponding resonator scale length would be half the value found for the top pair of spectra. Thus, while simple 1-d organ pipe models can explain some of the features of harmonic tremor, they do not appear to encompass all of the observed complexities of tremor behavior and should be applied with caution.

Julian (1994) developed a model for harmonic tremor based on non-linear excitation of the conduit walls by fluid flow through an irregular channel. The model does not require acoustic resonance of the fluid. Instead, harmonic oscillations are excited by a non-linear instability that develops when fluid flows through a constricted channel with elastic walls. An increase in the flow speed, either due to an increased

magma flux from below or a constriction in the channel causes the fluid pressure to decrease and the channel walls to move toward each other. This restricts the fluid flow, causing the pressure to increase and forcing the channel open again. The cycle repeats, eventually leading to limit-cycle oscillations characteristic of non-linear systems. This model appears to be able to explain many of the features of harmonic tremor observed at Arenal, in particular, the abrupt step-like transitions of the fundamental frequency from 2 to 1 Hz. Harmonic tremor is initiated when fluid flow through the channel exceeds a critical threshold, corresponding to a driving pressure of about 5 MPa. At higher driving pressures, the frequencies of tremor are observed to decrease, in step-like manner, to half their original values. At still higher pressures, tremor becomes chaotic and no longer exhibits harmonic peaks. The model also predicts an inverse relationship between tremor frequency and amplitude that is sometimes observed in the Arenal tremor data. This model is attractive because it explains the changing harmonic frequencies in terms of changing flow conditions in the conduit, rather than in terms of the changing dimension (length) of a stationary gas cavity, which does not appear to be consistent with observations of nearly identical tremor frequencies at volcanoes of very different size (e.g. Arenal, Semeru, Merapi, Sakurajima, Karymsky). In another paper in this volume, we examine several potential source models for the gliding tremor frequencies observed at Arenal (Garcés et al., 2000).

5.2. Tremor particle motion

Fig. 19 shows three-component particle motions for 30 s of tremor recorded at the five broadband sites. The particle motions are elliptical in all three planes and are not consistent with simple body waves, indicating the presence of surface waves and/or out-of-phase body waves. In fact, the seismic wavefield may not separate out into body and surface waves at these close distances. The tremor particle motions are generally complex and exhibit a radiation pattern that is not consistent with a radially symmetric radiator (e.g. a vertical cylinder), which radiates only P and SV waves, but may be consistent with a rectangular crack-like resonator, which is an efficient radiator of SH waves (Chouet et al., 1997). The observed particle motion ellipticity is not stationary but constantly rotates (Fig. 19). Similar elliptically rotating tremor particle motions have been reported at Sakurajima Volcano (Tsuruga et al., 1997), and the complicated nature of volcanic tremor particle motions has been commented upon by several authors [e.g. Kubotera (1974); Riedesel et al. (1982)], leading Fehler (1983) to conclude that a unique determination of the wavetypes that compose tremor is not possible. In general, tremor amplitudes are approximately twice as large on the horizontal components as on the verticals, and all amplitudes fall off rapidly with distance from the summit, in some instances, decaying faster than $1/r$. The tremor amplitude fluctuates with time by up to a factor of ten, yet the relative three-component amplitude ratios at a single station (N/Z, E/Z, N/E) remain nearly constant, as do the inter-station amplitude ratios (e.g. WARN Z/VACR Z). These observations suggest that the location of the tremor source is not changing appreciably with time. This differs from conclusions drawn by Benoit and McNutt (1997) who suggested that the tremor source at Arenal changes position with time. They computed the polarization of a “whoosh” event, described as an event that sounds like a jet plane and lasts 10–50 s (Melson, 1989), and is often followed by audible rhythmic gas emissions (“chugs”). They found that the fundamental peak of the harmonic tremor (1.9 Hz) is linearly polarized at N40W for the first 90 s following the explosion, and then abruptly rotates to N65E within a period of 12 s, while at the same time, the apparent incidence angle steepens. They attribute these changes in polarization to an S wave source that becomes progressively deeper with time.

We attempted to confirm these findings with our data. Fig. 20 shows the polarization computed at WARN for a small eruption similar to that described by Benoit and McNutt (1997). Polarization azimuth and incidence angle are computed from the eigenvectors of the covariance matrix (e.g. Jurkevics, 1988) within discrete windows which are shifted in time. The three-component seismograms have been bandpass filtered (0.5–3.2 Hz) to contain only the fundamental harmonic tremor peak (the spectrogram was computed from the unfiltered vertical velocity). We used a 10-s time window, shifted in 1.25 s steps for the polarization computations to correspond to the

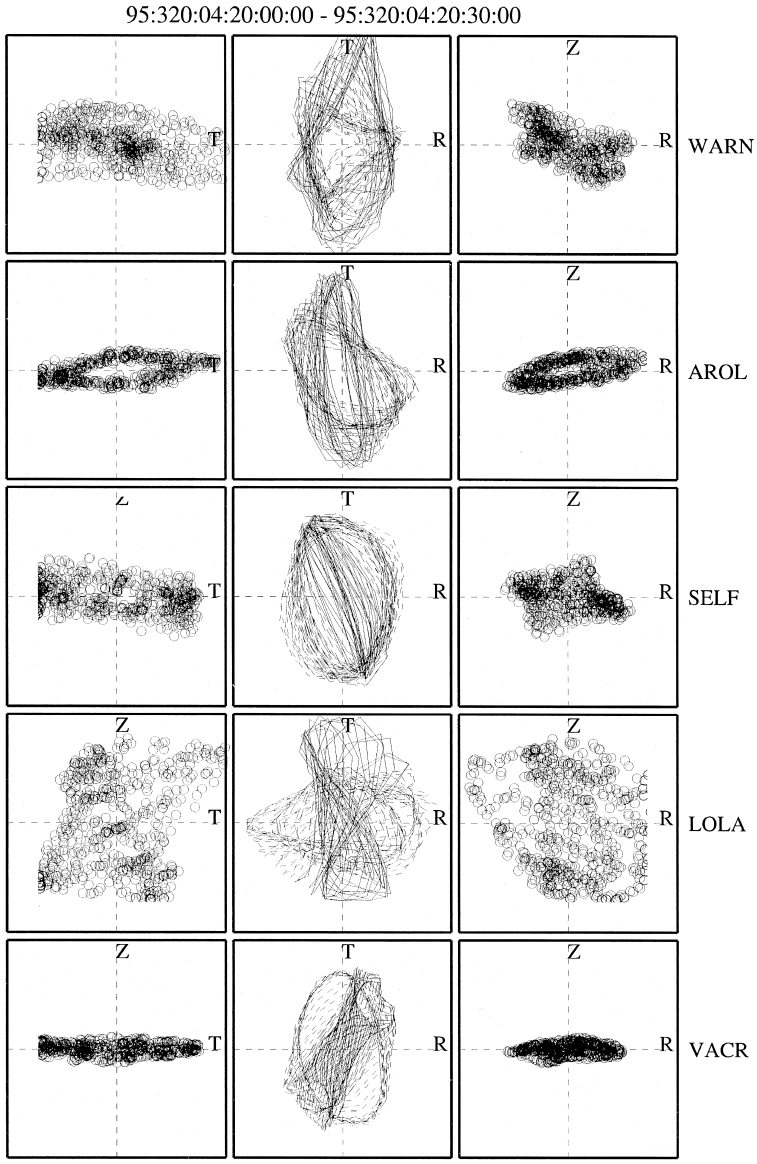

Fig. 19. Three-component particle motions (Z–T, T–R, and Z–R) for a 30 s tremor slice recorded at the five broadband stations. Line styles (dotted-solid-dashed) in T–R plane indicate successive 10 s time windows.

parameters used by Benoit and McNutt (1997). The results confirm our previous particle motion analysis (e.g. Fig. 19) and differ from Benoit and McNutt (1997) on several key points: (1) tremor is not linearly polarized; (2) tremor polarization is not stable for up to 90 s; and (3) tremor polarization does not appear to switch into a second stable mode. Rather, tremor polarization appears to be very complex (ellipsoidal) and continually changing (the polarization ellipsoid continually rotates about the origin).

If the source is deepening with time during an eruption as suggested, the effective length of the resonating column might be expected to increase, which should cause the fundamental frequency of observed harmonic tremor to decrease. However, the opposite effect is seen: the frequency glides to higher

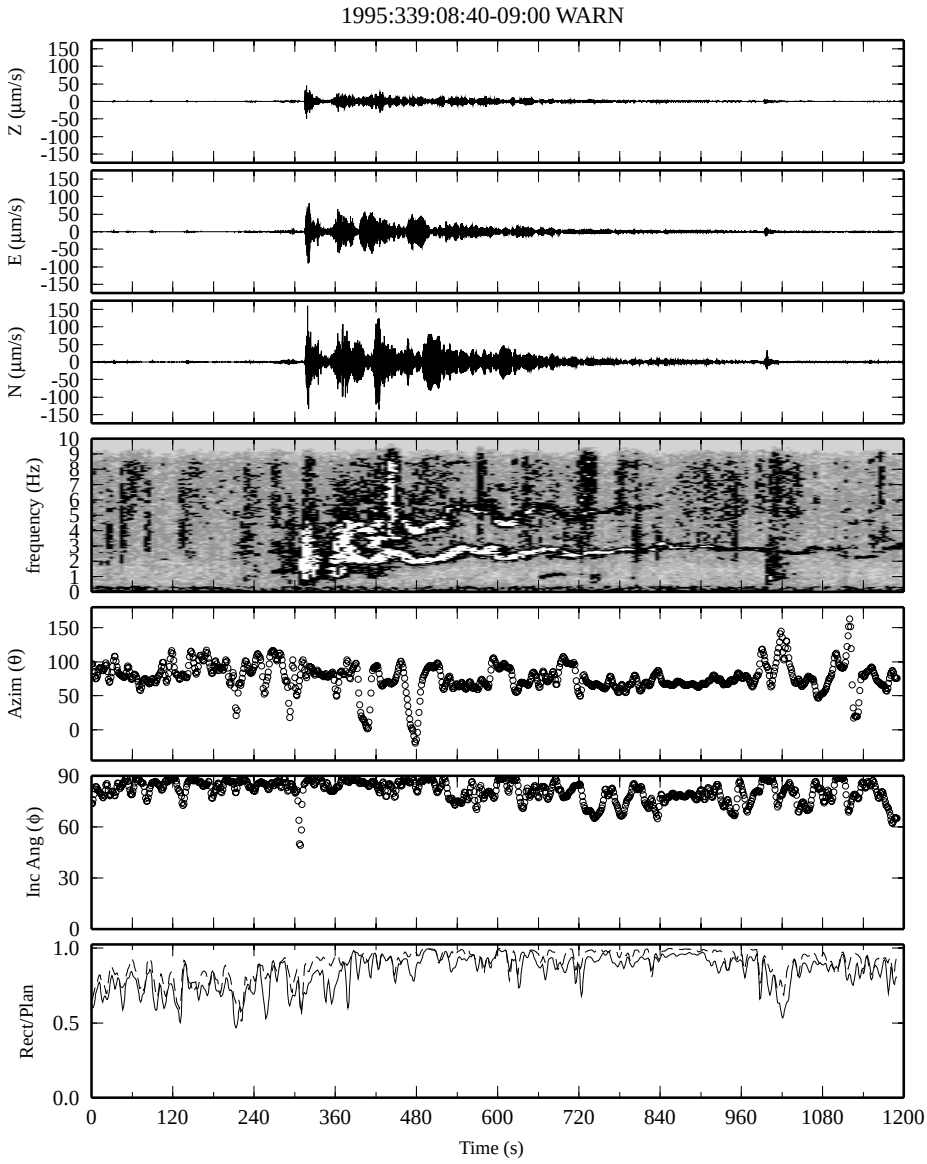

Fig. 20. Three component ground velocity (top three panels), vertical component spectrogram (middle panel) and polarization measures (bottom three panels) for a small explosion recorded at WARN. As indicated in Fig. 19, tremor polarization is not linear but complex and continually changing.

values (Fig. 20, middle panel). Nevertheless, the idea that the tremor wavefield is composed of SV and SH waves (S waves) incident at angles greater than the critical angle is a good one which does help to explain the complicated, elliptical particle motion. The interfering transverse and longitudinal modes of a two-dimensional crack can also produce elliptical particle motion (Chouet et al., 1997). It may not be possible, however, to isolate the relative contributions of the two effects (interfering crack modes and out-of-phase SH/SV waves) on the resulting elliptical particle motion.

As a final attempt to measure tremor polarization, we selected a period of time when the tremor

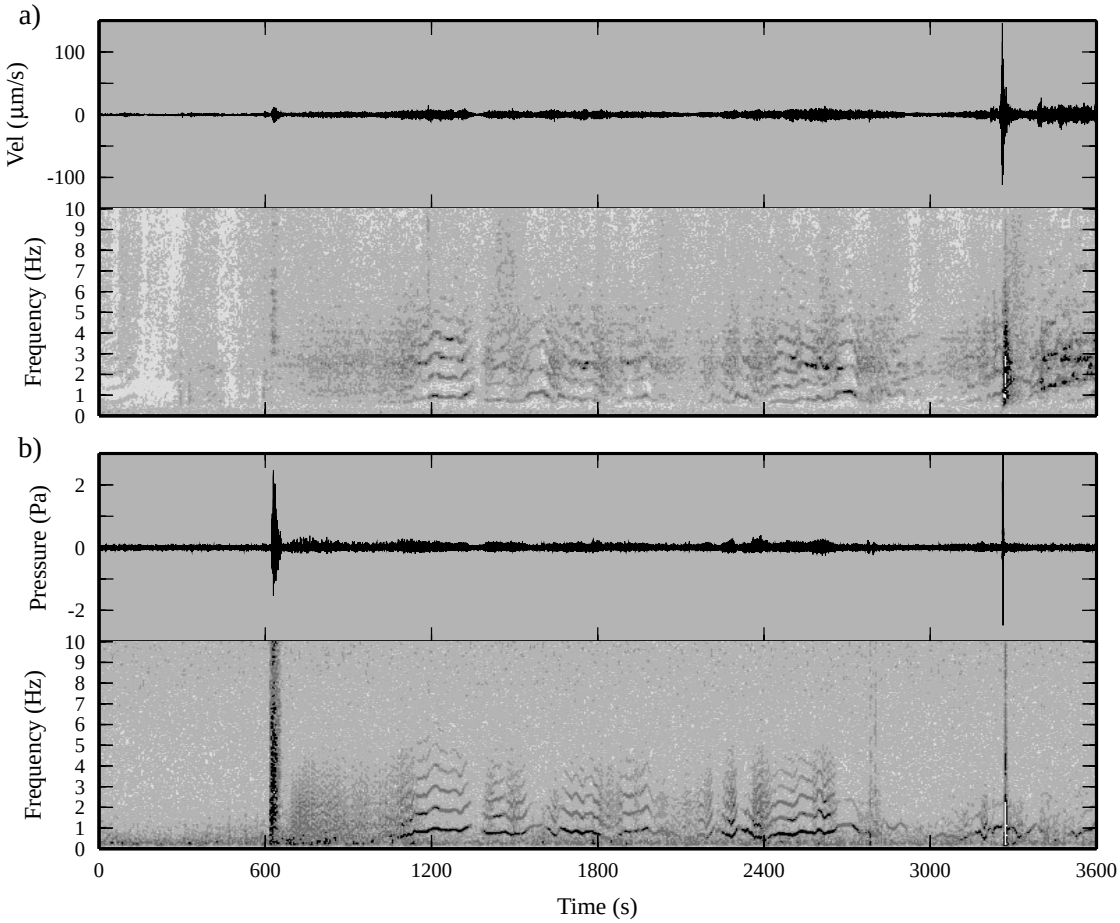

Fig. 21. (a) One hour of vertical velocity at WARN (top) and corresponding spectrogram (bottom). (b) Airborne acoustic pressure (top) and spectrogram (bottom) for the same period. Two summit explosions with different partitioning between the seismic and acoustic energy are separated by over 25 min of harmonic tremor that is clearly visible on both the seismic and acoustic channels.

consisted of a single frequency peak which steadily increased over time. Again, polarization was found to be complex and no orderly relationship between the frequency content and the polarization was observed. Eriditato and Luongo (1997) encountered similar instabilities in polarization azimuths of explosions recorded at Stromboli, which they attributed to complications of path structure and site topography. The extreme topography at Arenal undoubtedly influences polarization estimates.

5.3. Acoustic recordings of tremor

Several episodes of faint harmonic tremor were recorded by the seismometers during the array experiment. Some of these were also picked up by the condenser microphones. In addition, a period of small, regularly repeating explosions, presumably representing bursting of discrete gas bubbles, was recorded by both the seismometers and the microphones. In this section we analyze the seismic and acoustic recordings for a period of harmonic tremor and a period of repeating explosions in order to test the hypothesis that harmonic tremor represents a series of regularly repeating LP events.

5.3.1. Harmonic tremor

Fig. 21a shows one hour of the vertical component

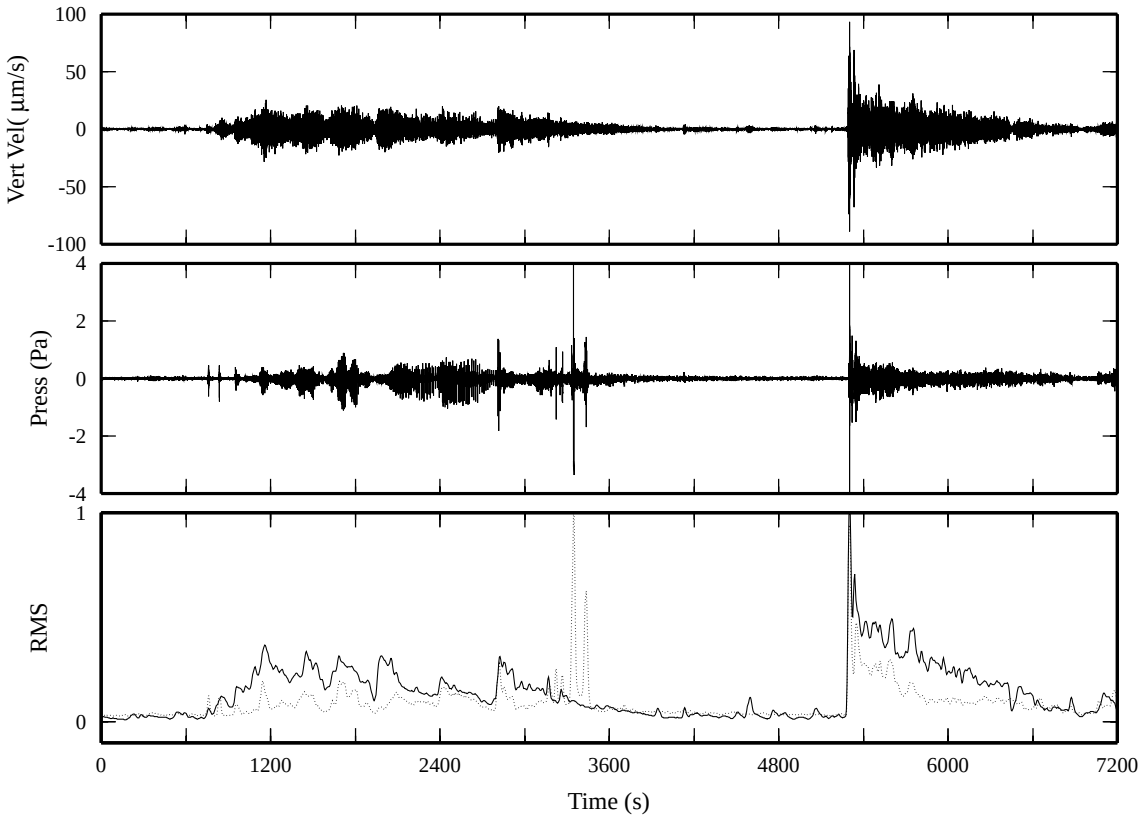

Fig. 22. Vertical velocity (top), acoustic pressure (middle), and RMS seismic (solid) and acoustic (dotted) energies (bottom) for the time period 117:03:30–05:30 recorded at WARN. Note the strong correlation between the acoustic and seismic RMS values, indicating good coupling between the seismic and acoustic wavefields.

of ground velocity recorded during our temporary seismo-acoustic array experiment (April–May 1997) by the broadband seismometer at WARN, approximately 2 km from the summit. Beneath the seismogram is the corresponding spectrogram, showing the log-normalized power spectral density as a function of time. Fig. 21b shows the acoustic air pressure recorded for the same period of time by a condenser microphone co-located with the seismometer, along with its spectrogram. Sandwiched between two explosions of different seismic efficiency are approximately 25 min of clear acoustic and seismic recordings of harmonic tremor. While a few researchers have noted a correlation between seismic and acoustic energy fluctuations during summit explosions and non-harmonic tremor bursts (Gordeev, 1992; Ripepe et al., 1996), these data are some of the first direct airborne pressure measurements of harmonic tremor ever reported. Sakai et al. (1996) and Johnson et al. (1998) recently report similar observations for Sakurajima and Karymsky volcanoes, respectively. Acoustic recordings are very important because they prove conclusively that the dominant features of seismically recorded harmonic tremor are not the result of reverberation within the shallow layers of the volcanic edifice (path effects), but rather, originate from pressure disturbances within the magma–gas mixture inside volcanic conduits.

However, we still have not identified the “source” of the tremor—whether it results from resonance of the magma–gas filled conduit, from shallow, regular bursting of small gas bubbles, from the flow of high-pressure gas through an orifice, or other flow-induced oscillations. One interpretation of the variable

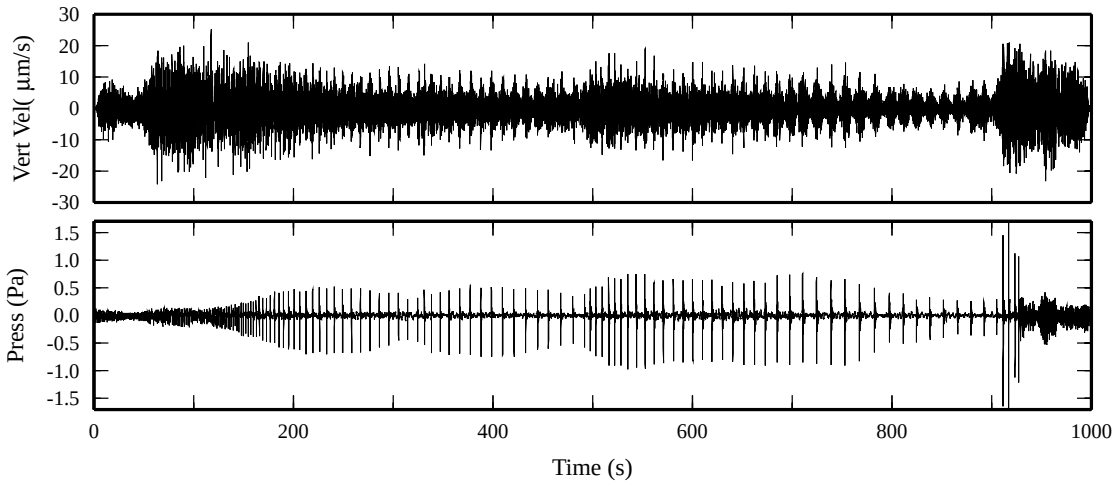

Fig. 23. Vertical velocity (top) and acoustic pressure (bottom) for a 1000 s period (117:04:01:40–04:18:20) windowed from the traces shown in Fig. 22.

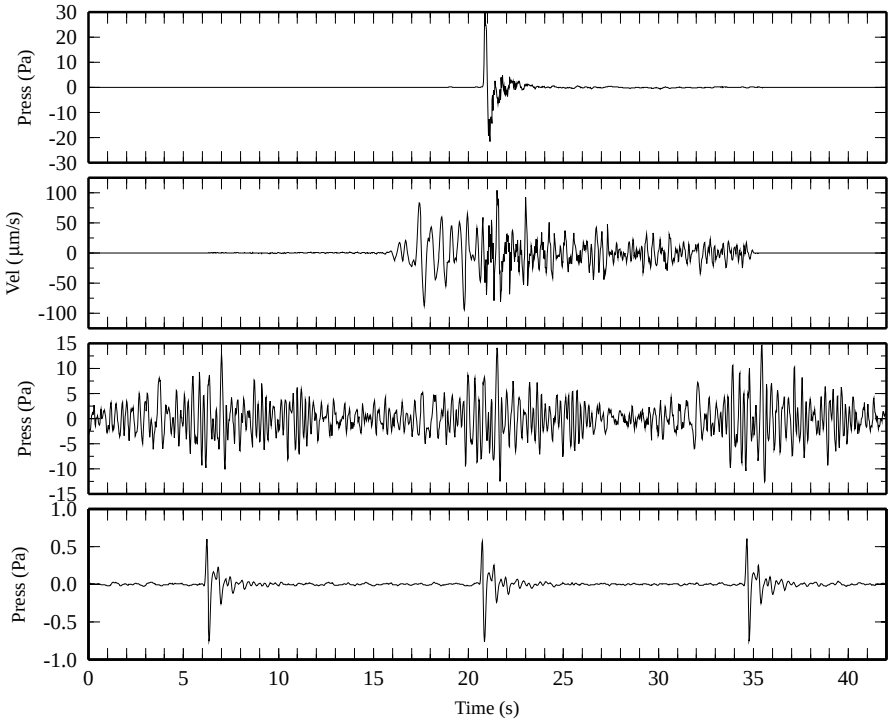

Fig. 24. Top: two traces: acoustic and seismic waveforms for the large summit explosion 122. Bottom two traces: acoustic and seismic waveforms for a zoomed in window taken from the explosion series shown in Fig. 23. Each seismic packet can be seen to correspond to an isolated explosion impulse in the acoustic channel.

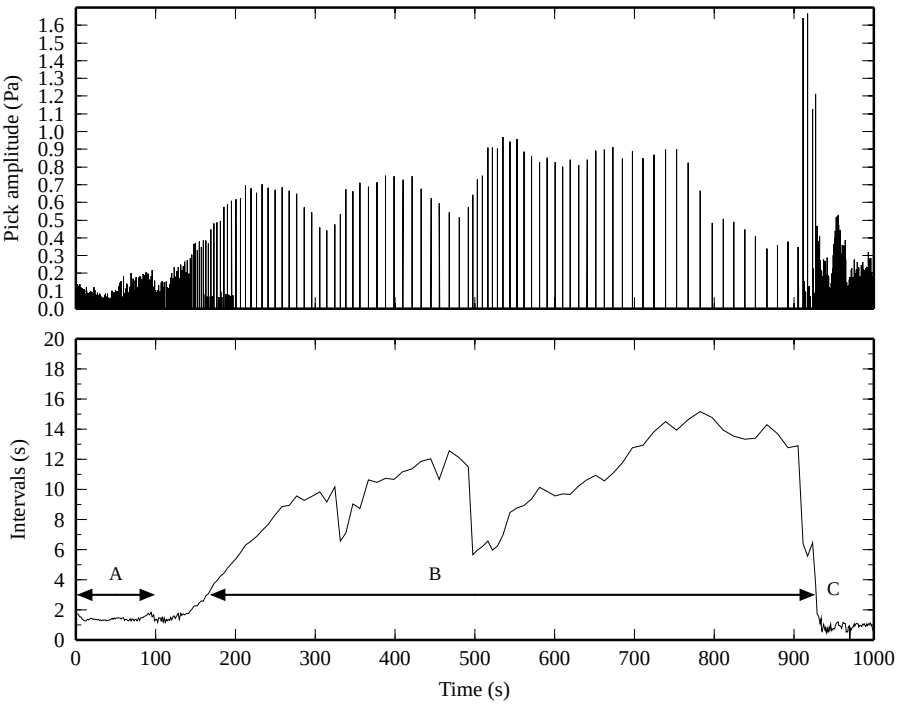

Fig. 25. Explosion impulses converted into individual picks (top) and the time interval between successive explosions (bottom) for the acoustic recording shown in Fig. 23. Note that during time periods A and C the explosion time interval is very stable.

efficiency and the gliding observed in Fig. 21 is that they are caused by a time-varying void fraction within the conduit which is produced by changing flow conditions (Garcés et al., 2000). Below we examine a period of regularly repeating explosions and contrast it with the harmonic tremor.

5.3.2. Repeated gas explosions

Fig. 22 shows a 2-h period of the vertical ground velocity and airborne acoustic pressure recorded at WARN approximately three hours before the harmonic tremor episode discussed above. Several bursts in the seismic channel are seen to precede a sharp summit explosion at ~5200 s. The last panel compares the seismic root-mean-squares (RMS) value (solid line) with the acoustic RMS (dotted line). The two large spikes at ~3300 s in the acoustic record are instrument noise. The close agreement between the acoustic and seismic RMS values indicates that the acoustic and seismic wavefields are well-coupled during this period. Fig. 23 shows a close-up of 1000 s from this period (between 1900–2900 s in Fig. 22). Each seismic burst can be seen to correspond to a small, isolated explosion impulse in the acoustic channel. The seismic packet generated by each small explosion, and its timing with respect to the airborne acoustic pulse recorded by the microphone, are very similar to those produced by large summit explosions (Fig. 24). The time between successive explosions varies from ~0.7–15 s throughout this period. This can be seen more clearly in Fig. 25 where the acoustic trace has been converted into a series of explosion picks. Beneath the pick series is a plot of the interval time between successive explosions. Note the close correspondence between the explosion amplitudes and the explosion intervals: As the explosions become larger they occur less frequently (larger repeat time), conserving the rate of acoustic energy released during degassing.

5.3.3. Repeat explosion model

In order to determine the stability of explosion

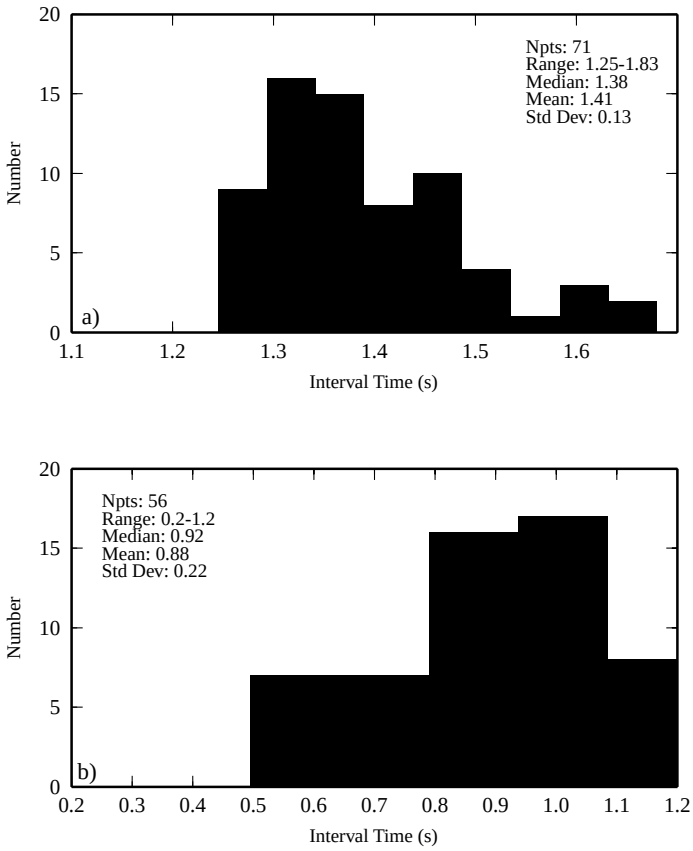

Fig. 26. (a) Histogram of 71 explosion interval times for the period 0–100 s("A" in Fig. 25). (b) Histogram of 56 explosion interval times for the period 950–1000 s ("C" in Fig. 25).

repeat times and to understand how these relate to harmonic tremor generation, we focus on two relatively stable periods (*A* and *C*, Fig. 25). A histogram of the interval times of 71 successive explosions that occurred during period *A* is plotted in Fig. 26a. The distribution of interval times is quasi-Gaussian, with a mean time of 1.41 s and a standard deviation (σ) of 0.13 s. Fig. 26b shows the distribution of interval times for period *C*; the explosions occur more frequently (mean = 0.88 s) than during period *A*, and with greater dispersion of interval times ($\sigma =$ 0.22 s), consistent with the larger variance in explosion amplitudes during this period (Fig. 25). While these explosions repeat quite regularly, particularly during period *A*, the corresponding acoustic and seismic spectra do not show the pronounced harmonic spectral peaks characteristic of harmonic tremor. This can be seen in Fig. 27 where we show 30 s windows of acoustic and seismic data taken from both the period of harmonic tremor (117:07:30) and the explosion series (117:04). The acoustic amplitudes for both periods are comparable (~0.1 Pa). The seismic amplitudes of the explosion series (~10 μm/s) are approximately twice as large as those of the harmonic tremor (~5 μm/s), indicating a higher seismic efficiency during the explosion series.

Fig. 27b shows the Fast-Fourier Transform (FFT) amplitude spectrum for each trace in Fig. 27a. Note the clear harmonic spectra in the acoustic and seismic channels. The fundamental frequency is around 1 Hz and at least five overtones can be discerned. The additional low frequency peak in the acoustic spectra (~0.2 Hz) may be due to a combination of

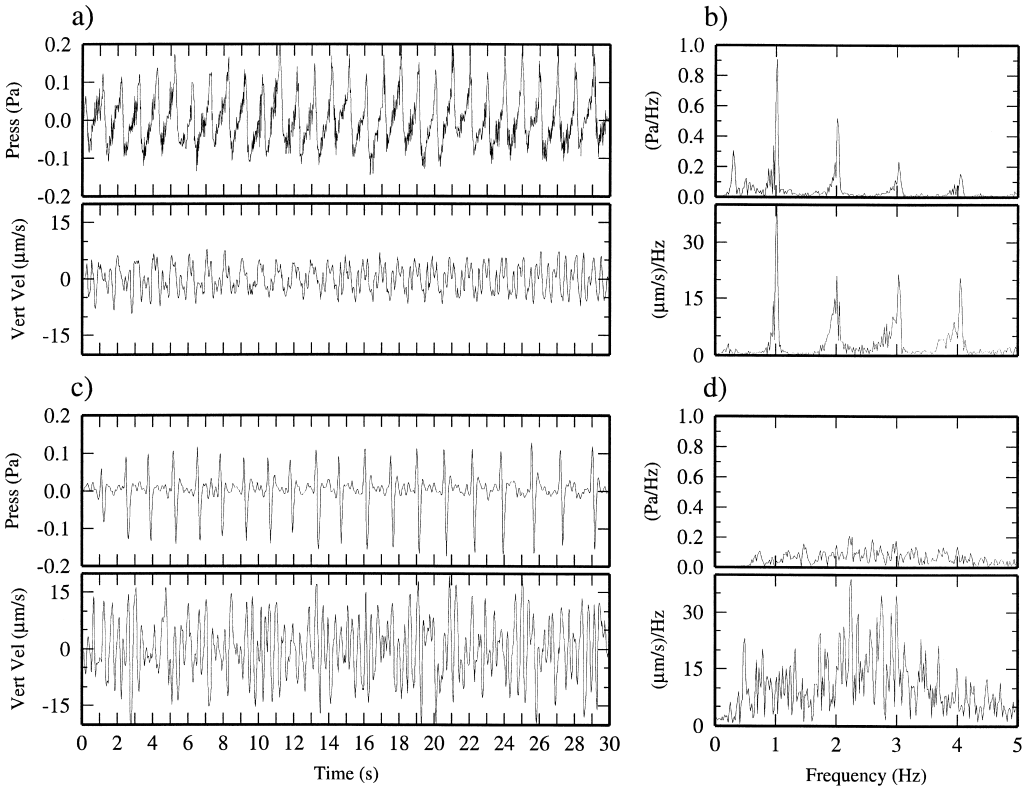

Fig. 27. (a) 30 s windows of harmonic tremor (117:07 GMT), recorded on acoustic and seismic channels at WARN. (b) Fourier amplitude spectra for panels in (a) plotted on a linear-linear scale. (c) 30 s windows of repeat explosions (1997:04 GMT), recorded on acoustic and seismic channels at WARN. (d) Fourier amplitude spectra for panels in (c) plotted on a linear-linear scale. Note the clear difference in the spectra between the harmonic tremor (b) and the repeat explosions (d).

mountain-generated noise recorded on the leeward side of the volcano, and noise from the microphone low-frequency adaptor which was not fully removed by filtering. The bottom two panels (Fig. 27d) show the acoustic and seismic spectra for the repeated explosions shown in Fig. 27c. While there are some common peaks between these spectra and the harmonic spectra (e.g. 3 and 4 Hz), the spectra corresponding to repeated explosions are not harmonic. A series of impulses spaced τ s apart will have a Fourier Transform amplitude spectrum that consists of a series of frequency peaks spaced τ^{-1} Hz apart. Because of the appearance of the resulting frequency spectrum, this is termed the 'comb effect' (Bracewell, 1986). The envelope of the explosion series spectrum (Fig. 27d) has the appearance of spectral envelopes of larger explosions, roughed up by a 'dirty comb'. Apparently the explosion repeat intervals are not sufficiently regular to produce harmonic spectra via the comb effect.

Several studies have extended the notion that tremor represents a superposition of LP events by noting that seismic LP events can be generated by shallow, gas bubble bursts. Based on the similarity of tremor and LP earthquake waveforms, Fehler (1983) proposed that volcanic tremor is composed of a series of LP earthquakes. Gordeev (1993) suggested that harmonic tremor results from a succession of impulses (comb effect) generated by discrete gas explosions within the volcanic crater. Ripepe et al. (1996) measured small (~1 Pa) acoustic impulses at Stromboli with a dynamic microphone placed 150 m from the active vent. Video images confirmed that the regularly repeating acoustic pulses were associated with small gas bursts. The delay times between bursts were measured for one hour and found to have a

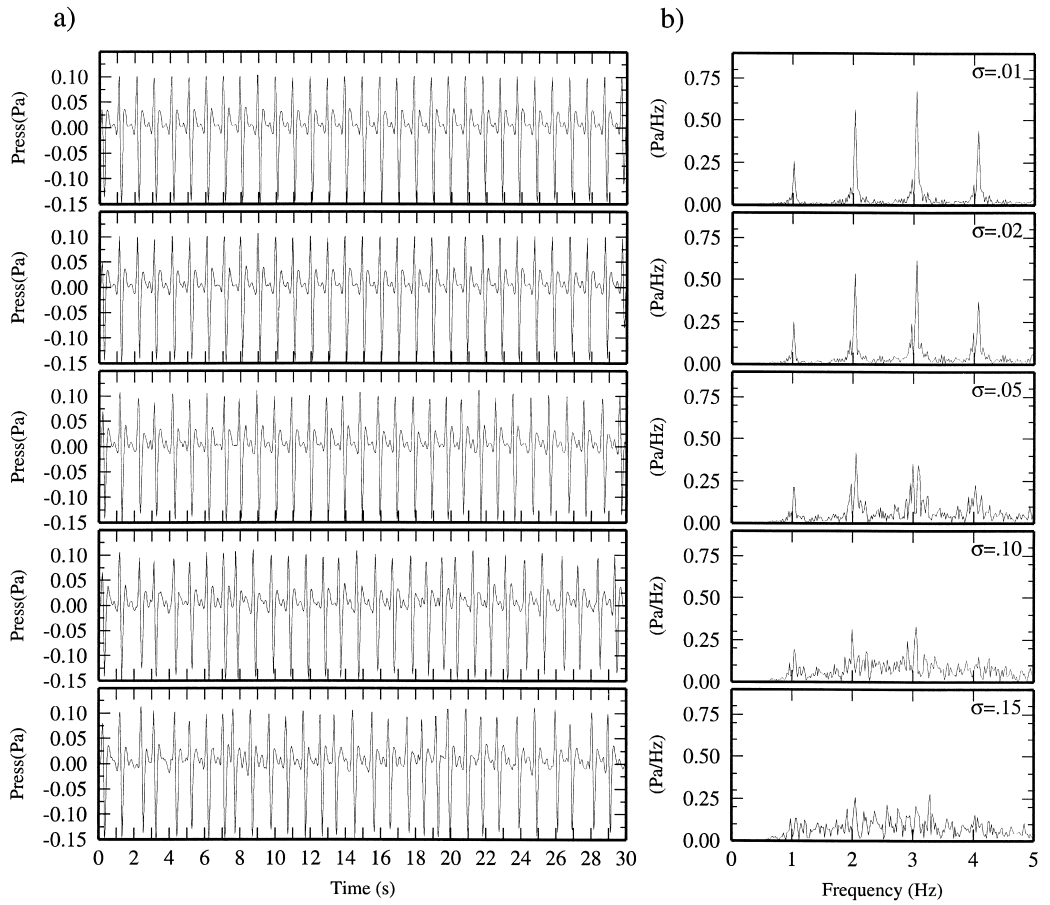

Fig. 28. (a) Synthetic time series produced by superposing an acoustic impulse (windowed from the data shown in Fig. 27c and labelled "pulse a" in Fig. 13) with a mean repeat time of 1 s and variable repeat time standard deviations (σ) of 0.01–0.15 as indicated in (b). (b) Spectra for the synthetic time series shown in (a). Note that only repeat times with standard deviations of less than 0.1 generate harmonic spectra.

Gaussian distribution with a mean delay time of 1 s and a standard deviation of 0.096 s. They attributed volcanic tremor at Stromboli to this continuous bursting of gas bubbles and suggested that more stable repeat intervals gives rise to harmonic tremor via the comb effect.

In order to assess how regular the intervals between successive explosions must be to generate harmonic spectra via the comb effect, we formed synthetic records of repeated bursts. An acoustic pulse was isolated from the repeat explosion series ("pulse a" in Fig. 13) and was superposed with variable repeat intervals to form a 30 s long synthetic pulse train. The repeat intervals were determined by generating a random Gaussian distribution of interval times with a mean value of 1 s and a variable standard deviation which was determined for each synthetic run. Fig. 28a shows the resulting synthetic traces for $\sigma = 0.01 - 0.15$ s; the corresponding FFT spectra are shown in Fig. 28b. In order to generate harmonic tremor peaks with the signal-to-noise seen in the data, the standard deviation of explosion repeat times must be very small ($\sigma < 1\%$). The explosion repeat intervals observed at both Stromboli and Arenal have a much larger variance than this ($\sigma \sim 10 - 20\%$), even over periods as short as 30 s. It seems highly improbable that regularly repeating shallow gas explosions produce harmonic tremor observed at Arenal, which often persists for several hours. Another observation that would seem to rule out the superposition model of

harmonic tremor is gliding. The harmonic tremor frequencies shift while maintaining their regular spacing (glide) over very short periods of time—the precise timing needed to do this via smoothly changing the interval time between successive explosions seems inconsistent with the observed variance in explosion repeat times. A final argument against the superposition model is the acoustic and seismic spectral envelopes (Fig. 27). The synthetic tests demonstrate the well-known result of the comb effect that the Fourier transform of a series of regularly repeated impulses has the same spectral envelope as an individual impulse. While peak frequencies of Arenal tremor are very stable, the spectral envelopes change quite a bit. If the superposition model were correct, these changes would correspond to drastic changes in the spectra of individual explosions, which are not observed. In fact, we observe a remarkable stability in the individual explosion waveform spectra recorded at a particular site (Fig. 4). Thus, while harmonic tremor and repeated gas explosions likely share a similar source region, they must differ in their excitation and feedback mechanisms. This conclusion is expected to hold at other volcanoes where harmonic tremor is observed to persist for hours to days, including Karymsky, Sakurajima, Mt. Semeru, Langila, and Merapi volcanoes. It is however possible that quasi-regularly repeating bubble bursts could be responsible for non-harmonic or spasmodic tremor, as suggested by Ripepe (1996) and others. A recent study of seismicity associated with White Island volcano found that non-harmonic tremor is correlated with shallow surface activity such as bubble bursting and crater formation, while harmonic tremor is not related to surface activity and presumably has a deeper source (Sherburn et al., 1998). Our results, presented above, corroborate this; a deeper and/or extended source explains why, in contrast to the shallow summit explosions, harmonic tremor displays no seismic site effect. In the non-linear flow excitation model (Julian, 1994), harmonic tremor occurs when the driving pressure reaches a critical threshold, while non-harmonic tremor occurs for both lower and higher pressures.

6. Conclusions

We have presented a comprehensive analysis of seismic and acoustic data observed at Arenal Volcano, Costa Rica, over the past three years. In the process, we have compared our observations at Arenal to those at several other volcanoes (e.g. Stromboli, Merapi, Langila, Karymsky, Sakurajima, Semeru, White Island) in an attempt to show that the similarities between recent, high-quality seismic observations at different active volcanoes greatly outweigh the differences. During this period (1995–1997), Arenal's eruptive behavior has been remarkably stable, characterized by small strombolian summit explosions occurring roughly every 30 min. Seismic signals recorded at Arenal are primarily of two types: LP transients (1–3 Hz) associated with summit explosions, and nearly continual harmonic tremor containing regularly spaced spectral peaks (0.9, 1.8, 2.7, 3.6, 4.5, 5.4, 6.3 and 7.1 Hz). In contrast to tremor, the summit explosions exhibit distinct temporal and spectral signatures at each site, suggesting significant path and/or site modification of the waveforms. However, the explosion process is highly repeatable, producing nearly identical waveforms at a given station. Through waveform cross-correlation with a master event we have determined that the explosion source location does not change appreciably over time. Both timing of seismic and acoustic phases and acoustic waveform modeling suggest that explosions occur at very shallow depth beneath the summit, and that the seismic and acoustic explosion sources are coincident. The acoustic waveforms of summit explosions are found to be much more impulsive than the seismic waveforms, and on a greatly magnified scale, to contain evidence of precursory system 'priming'. The seismic efficiency of explosions is observed to vary greatly and may indicate changing conditions within the conduit such as a time-varying void fraction. The good coherence of explosion waveforms across the radial array allowed the identification of seismic phases moving with phase velocities of 3.1, 1.3, and 0.6 km/s, and believed to represent P, SV, and Love waves, respectively. Polarization analyses of these phases were, however, inconclusive. Seismic polarization appears to be greatly affected by propagation through the complex volcanic structure.

Harmonic tremor has been simultaneously recorded on the acoustic and seismic channels. This and the lack of variation in the frequency content of harmonic tremor at different seismic sites prove conclusively

that it is not a seismic propagation effect. Tremor particle motions are primarily elliptical and suggest a mixture of SH and SV waves arriving at near critical incidence. Tremor polarization is chaotic and does not appear to be simply related to tremor frequency. Closely related signals, believed to represent discrete gas bubble bursts at shallow depths, were also recorded. However, the repeat times of these quasi-regular explosions are not sufficiently regular to produce harmonic spectra via the comb effect. Synthetic tests show that explosion repeat times must be exceedingly regular to produce harmonic tremor. This, and the absence of explosion spectral envelopes in the harmonic tremor spectra, suggest that sustained harmonic tremor is probably not generated by regularly repeating shallow gas explosions, although its mechanism is expected to be closely related.

Acknowledgements

We thank the entire staff of the Volcanological and Seismological Observatory (OVSICORI) of the National University of Costa Rica, whose help made this project possible. In particular, Vilma Barboza, Eliecer Duarte, Erick Fernandez, Enrique Hernández, Antonio Mata, Daniel Rojas, and Rodolfo Van der Laat of OVSICORI, and Dan Sampson of UCSC, assisted with vault constructions and the data collection. Field deployments were facilitated by the hospitality of the Arenal Observatory Lodge. Fabio Cedeño and the Arenal Volcano National Park granted access to favorable observation sites. John Lahr generously provided his hypocentral determination code (Hypoellipse), and the Stanford IRIS-PASSCAL instrument center graciously loaned us L22s. The figures in this paper were made with GMT; we thank P. Wessel and W. Smith for making this useful program available to all. This work was partially supported by an NSF graduate fellowship to MTH and NSF grant No. EAR-9614687 to SYS. Contribution 361 of the Institute of Tectonics and the W. M. Keck Seismological Laboratory, University of California, Santa Cruz.

References

Bracewell, R.N., 1986. The Fourier Transform and its Applications, McGraw-Hill, New York.

Benoit, J.P., McNutt, S.R., 1997. New constraints on source processes of volcanic tremor at Arenal Volcano, Costa Rica, using broadband seismic data. Geophys. Res. Lett. 24 (4), 449–452.

Borgia, A., Poore, C., Carr, M.J., Melson, W.G., Alvarado, G.E., 1988. Structural, stratigraphic, and petrologic aspects of the Arenal–Chato volcanic system, Costa Rica; evolution of a young stratovolcanic complex. Bull. Volcanol. 50 (2), 86–105.

Braun, T., Ripepe, M., 1993. Interaction of seismic and air waves recorded at Stromboli Volcano. Geophys. Res. Lett. 20 (1), 65–68.

Buckingham, M.J., Garcés, M.A., 1996. A canonical model of volcano acoustics. J. Geophys. Res. 101 (4), 8129–8151.

Chouet, B., 1996. Long-period volcano seismicity: its source and use in eruption forecasting. Nature 380 (6572), 309–316.

Chouet, B.A., Saccorotti, G., Martini, M., Dawson, P., De Luca, G., Milana, G., Scarpa, R., 1997. Source and path effects in the wave fields of tremor and explosions at Stromboli Volcano, Italy. J. Geophys. Res. 102 (7), 15 129–15 150.

Ereditato, D., Luongo, G., 1997. Explosion quakes at Stromboli (Italy). J. Volcanol. Geotherm. Res. 79, 265–276.

Fehler, M., 1983. Volcanictremor at Mount St. Helens Volcano. J. Geophys. Res. 88, 3476–3484.

Frémont, M.J., Malone, S.D., 1987. High precision relative locations of earthquakes at Mount St. Helens, Washington. J. Geophys. Res. 92 (B10), 10 223–10 236.

Garcés, M.A., Hansen, R.A., 1998. Waveform analysis of seismoacoustic signals radiated during the Fall eruption of Pavlof volcano, Alaska. Geophys. Res. Lett. 25 (7), 1051–1054.

Garcés, M.A., McNutt, S.R., 1997. Theory of the airborne sound field generated in a resonant magma conduit. J. Volcanol. Geotherm. Res. 78, 155–178.

Garcés, M.A., Hagerty, M.T., Schwartz, S.Y., 1998. Magma acoustic and time-varying melt properties at Arenal Volcano, Costa Rica. Geophys. Res. Lett. 25 (13), 2293–2296.

Garcés, M.A., Hagerty, M.T., Schwartz, S.Y., 2000. On the generation and radiation of harmonic tremor at Arenal Volcano: a synergy of fluid flow, sound and vibration. J. Volcanol. Geotherm. Res., in press.

Gordeev, E., 1992. Modelling of volcanic tremor wave fields. J. Volcanol. Geotherm. Res. 51, 145–160.

Gordeev, E., 1993. Modeling of volcanic tremor as explosive point sources in a single-layered, elastic half-space. J. Geophys. Res. 98 (B11), 19 687–19 703.

Hagerty, M.T., Schwartz, S.Y., Protti, M., Garcés, M., Dixon, T., 1997. Observations at Costa Rican volcano offer clues to causes of eruptions. Eos Trans. AGU (570–571) 78 (49), 565.

Ishihara, K., 1985. Dynamical analysis of volcanic explosion. J. Geodynamics 3, 327–349.

Johnson, J.B., Lees, J.M., Gordeev, E.I., 1998. Degassing explosions at Karymsky Volcano. Kamchatka. Geophys. Res. Lett. 25 (21), 3999–4002.

Julian, B.R., 1994. Volcanic tremor—nonlinear excitation by fluid flow. J. Geophys. Res. 99 (B6), 11 859–11 877.

Jurkevics, A., 1988. Polarization analysis of three-component array data. Bull. Seismol. Soc. Am. 78, 1725–1743.

Kawakatsu, H., Ohminato, T., Ito, H., 1994. 10s-period volcanic tremors observed over a wide area in southwestern Japan. Geophys. Res. Lett. 21, 1963–1966.

Kieffer, S.W., Sturtevant, B., 1984. Laboratory studies of volcanic jets. J. Geophys. Res. 89, 8253–8268.

Kubotera, A., 1974. Volcanic tremors at Aso Volcano. In: Civetta, L., Gasparini, P., Luongo, G., Rapolla, A. (Eds.), Physical Volcanology. Elsevier, Amsterdam, Netherlands, pp. 29–47.

Lahr, J. C., 1989. HYPOELLIPSE/Version 2.0: A computer program for determining local earthquake hypocentral parameters, magnitude, and first motion pattern. US Geol. Surv., Open-File Rep. 89-0116.

Lahr, J.C., Chouet, B.A., Stephens, C.D., Power, J.A., Page, R.A., 1994. Earthquake classification, location, and error analysis in a volcanic environment: implications for the magmatic system of the 1989–1990 eruptions at Redoubt Volcano, Alaska. J. Volcanol. Geotherm. Res. 62, 137–151.

Lighthill, J., 1978. Waves in Fluids, Cambridge Press, New York.

Matumoto, T., Umana, J., 1976. Eruption of Arenal Volcano, Costa Rica and prediction of an eruption implied from seismic data. EOS, Spring Suppl. 57 (4), 347.

McNutt, S.R., 1986. Observations and analysis of B-type earthquakes, explosions, and volcanic tremor at Pavlof Volcano, Alaska. Bull. Seismol. Soc. Am. 76 (1), 153–175.

McNutt, S.R., 1989. Volcanic tremor from around the world. Bull. New Mex. Bureau Mines Min. Res. 131, 183.

Melson, W., 1989. Las erupciónes del volcán Arenal; 1 al 13 de abril de 1 9 8 9. Bol. de Vulc. 20, 15–22.

Minakami, T., Utibori, S., Hiraga, S., 1969. The 1978 Eruption of Volcano Arenal, Costa Rica. Bull. Earthquake Res. Inst. 47, 783–802.

Mori, J., Patia, H., McKee, C., Itikarai, I., Lowenstein, P., de Saint Ours, P., Talai, B., 1989. Seismicity associated with eruptive activity at Langila Volcano, Papua New Guinea. J. Volcanol. Geotherm. Res. 38, 243–255.

Murase, T., McBirney, A.R., 1973. Properties of some common igneous rocks and their melts at high temperatures. Geol. Soc. Am. Bull. 84, 3563–3592.

Neuberg, J., Luckett, R., Ripepe, M., Braun, T., 1994. Highlights from a seismic broadband array on Stromboli. Geophys. Res. Lett. 21, 749–752.

Press, F., Ewing, M., 1951. Theory of air-coupled flexural waves. J. Appl. Phys. 22, 892–899.

Press, F., Oliver, J., 1955. Model study of air-coupled surface waves. J. Acous. Soc. Am. 27, 43–46.

Riedesel, M., Orcutt, J., Macdonald, K., McClain, J., 1982. Microearthquakes in the Black Smoker hydrothermal field, East Pacific Rise at 21°N. J. Geophys. Res. 87, 10 613–10 623.

Ripepe, M.R., 1996. Evidence for gas influence on volcanic seismic signals recorded at Stromboli. J. Volcanol. Geotherm. Res. 70, 221–233.

Ripepe, M., Poggi, P., Braun, T., Gordeev, E., 1996. Infrasonic waves and volcanic tremor at Stromboli. Geophys. Res. Lett. 23 (2), 181–184.

Rowe, C.A., Aster, R.C., Kyle, P.R., Schlue, J.W., Dibble, R.R., 1998. Broadband seismic recordings of strombolian explosions and associated ultra-long-period signals on Mount Erebus, Ross Island, Antarctica. Geophys. Res. Lett. 25 (13), 2297–2300.

Sakai, T., Yamasato, H., Uhira, K., 1996. Infrasound accompanying C-type tremor at Sakurajima volcano (in Japanese). Kazan 41, 181–185.

Sassa, K., 1935. Volcanic micro-tremors and eruptive-earthquakes (Part 1 of the geophysical studies on the volcano Aso). Mem. Coll. Sci. Kyoto Univ. 18, 255–293.

Schlindwein, V., Wassermann, J., Scherbaum, F., 1995. Spectral analysis of harmonic tremor signals at Mt. Semeru volcano, Indonesia. Geophys. Res. Lett. 22, 1685–1688.

Sherburn, S., Scott, B.J., Nishi, Y., Sugihara, M., 1998. Seismicity at White Island volcano, New Zealand: a revised classification and inferences about source mechanism. J. Volcanol. Geotherm. Res. 83, 287–312.

Sparks, R.S.J., 1997. Causes and consequences of pressurisation in lava dome eruptions. Earth Planet. Sci. Lett. 150, 177–189.

Spudich, P., Cranswick, E., 1984. Direct observation of rupture propagation during the Imperial Valley earthquake using a short baseline accelerometer array. Bull. Seismol. Soc. Am. 74 (6), 2083–2114.

Tsuruga, K., Yomogida, K., Honda, S., Ito, H., Ohminato, T., Kawakatsu, H., 1997. Spatial and temporal variations of volcanic earthquakes at Sakurajima Volcano, Japan. J. Volcanol. Geotherm. Res. 75, 337–358.

Vergniolle, S., Brandeis, G., 1996. Strombolian explosions 1. A large bubble breaking at the surface of a lava column as a source of sound. J. Geophys. Res. 101 (B9), 20 443–20 447.

Wallis, G.B., 1969. One-dimensional Two Phase Flow. McGraw-Hill, New York.

Weill, A., Brandeis, G., Vergniolle, S., Baudin, F., Bilbille, J., Fevre, J., Piron, B., Hill, X., 1992. Acoustic sounder measurements of the vertical velocity of volcanic jets at Stromboli Volcano. Geophys. Res. Lett. 19, 2357–2360.